Monthly Notices
of the
ROYAL ASTRONOMICAL SOCIETY

MNRAS **472,** 1659–1676 (2017)
Advance Access publication 2017 August 12

doi:10.1093/mnras/stx2030

Improved measurements of turbulence in the hot gaseous atmospheres of nearby giant elliptical galaxies

A. Ogorzalek,[1,2]★ I. Zhuravleva,[1,2] S. W. Allen,[1,2,3] C. Pinto,[4] N. Werner,[5,6] A. B. Mantz,[1,2] R. E. A. Canning,[1,2] A. C. Fabian,[4] J. S. Kaastra[7,8] and J. de Plaa[7]

[1]*Department of Physics, Stanford University, 382 Via Pueblo Mall, Stanford, CA 94305-4060, USA*
[2]*Kavli Institute for Particle Astrophysics and Cosmology, Stanford University, 452 Lomita Mall, Stanford, CA 94305-4085, USA*
[3]*SLAC National Accelerator Laboratory, 2575 Sand Hill Road, Menlo Park, CA 94025, USA*
[4]*Institute of Astronomy, Madingley Road, CB3 0HA Cambridge, UK*
[5]*MTA-Eötvös University Lendület Hot Universe Research Group, Pázmány Péter sétány 1/A, Budapest 1117, Hungary*
[6]*Department of Theoretical Physics and Astrophysics, Faculty of Science, Masaryk University, Kotlářská 2, Brno 611 37, Czech Republic*
[7]*SRON Netherlands Institute for Space Research, Sorbonnelaan 2, NL-3584 CA, Utrecht, The Netherlands*
[8]*Leiden Observatory, Leiden University, PO Box 9513, NL-2300 RA, Leiden, The Netherlands*

Accepted 2017 August 3. Received 2017 August 3; in original form 2017 February 14

ABSTRACT

We present significantly improved measurements of turbulent velocities in the hot gaseous haloes of nearby giant elliptical galaxies. Using deep *XMM–Newton Reflection Grating Spectrometer* (*RGS*) observations and a combination of resonance scattering and direct line broadening methods, we obtain well bounded constraints for 13 galaxies. Assuming that the turbulence is isotropic, we obtain a best-fitting mean 1D turbulent velocity of $\sim$110 km s^{-1}. This implies a typical 3D Mach number $\sim$0.45 and a typical non-thermal pressure contribution of $\sim$6 per cent in the cores of nearby massive galaxies. The intrinsic scatter around these values is modest – consistent with zero, albeit with large statistical uncertainty – hinting at a common and quasi-continuous mechanism sourcing the velocity structure in these objects. Using conservative estimates of the spatial scales associated with the observed turbulent motions, we find that turbulent heating can be sufficient to offset radiative cooling in the inner regions of these galaxies ($<$10 kpc, typically 2–3 kpc). The full potential of our analysis methods will be enabled by future X-ray micro-calorimeter observations.

Key words: radiative transfer – turbulence – techniques: spectroscopic – galaxies: clusters: intracluster medium – galaxies: kinematics and dynamics – X-rays: galaxies: clusters.

1 INTRODUCTION

Giant elliptical galaxies are filled with hot ($\sim 10^7$ K), X-ray emitting gas. Various physical processes, e.g. galaxy mergers, supernova explosions and AGN activity, can perturb this gas and induce gas motions. These motions transport energy, mass and metals, influencing the thermodynamic state of galaxies. Therefore, measurements of X-ray gas velocities are crucial for understanding galaxy formation and evolution (e.g. Sijacki et al. 2007; Weinberger et al. 2017), radio-mechanical AGN feedback (e.g. Brüggen, Ruszkowski & Hallman 2005; Scannapieco & Brüggen 2008) and transport processes (e.g. Roediger et al. 2013; Kunz, Schekochihin & Stone 2014).

A direct way to probe gas velocity field is by measuring spectral line broadening (differential motions) and shifts in line centroids (bulk velocities). Recently, the *Hitomi* satellite measured a velocity broadening of 187 $\pm$ 13 km s^{-1} in the inner 30 kpc of Perseus cluster, where the galaxy NGC 1275 resides (Hitomi Collaboration et al. 2016). If these motions come from turbulence triggered by AGN-blown bubbles (on 20–30 kpc scales), then the associated heat dissipation would be sufficient to offset radiative cooling (Hitomi Collaboration et al. 2016). This result is consistent with the velocity structure inferred from the analysis of X-ray surface brightness fluctuations in the Perseus cluster (Zhuravleva et al. 2014; see also results for the Virgo and Centaurus clusters by Zhuravleva et al. 2014; Walker, Sanders & Fabian 2015).

For most giant elliptical galaxies and clusters, however, detailed gas velocity information is lacking. Additional measurements, extending to more systems, are vital to better understand the role of turbulent heating, as well as other processes, such as weak shocks and sound waves (e.g. Fabian et al. 2006; Randall et al. 2015; Fabian et al. 2017), cosmic ray heating (e.g. Guo & Oh 2008; Sijacki et al. 2008; Jacob & Pfrommer 2017; Ruszkowski, Yang & Reynolds 2017), bubble mixing (e.g. Hillel & Soker 2016),

★ E-mail: ogoann@stanford.edu

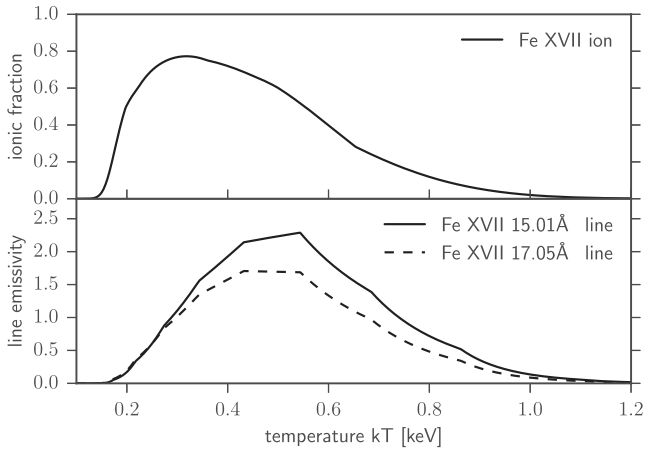

Figure 1. The ionic fraction of Fe XVII (upper panel) and the emissivity of the considered Fe XVII lines (arbitrary units) as a function of plasma temperature, calculated using the APEC model for optically thin plasmas (Smith et al. 2001; Foster et al. 2012) with AtomDB data base ver. 2.0.2.

radiative heating (e.g. Nulsen & Fabian 2000) and turbulent mixing (e.g. Kim & Narayan 2003).

The compact, cool, X-ray bright galaxies can be analysed using high resolution X-ray spectra from *Reflection Grating Spectrometer* (*RGS*). Applying it to a sample of group central galaxies, Sanders & Fabian (2013) and Pinto et al. (2015) provided velocity upper limits of $\sim$300 km s^{-1}. A major systematic uncertainty associated with the spatial extent of the source, which additionally broadens the spectral lines, typically limits these constraints to upper bounds only.

A promising indirect method of probing gas motions is resonant scattering effect. The X-ray emitting gas in elliptical galaxies is optically thin in the continuum and most line emission (i.e. the optical depth for free–free absorption is $\tau \sim 10^{-29}$ and is $\sim 10^{-2}$ for Thomson scattering). However, in the X-ray brightest resonance lines of abundant ions, the optical depth can be greater than one (Gilfanov, Syunyaev & Churazov 1987). This causes photons to be absorbed and then quickly re-emitted, leading to line flux suppression in a galaxy or cluster core (e.g. Shigeyama 1998). Small-scale turbulent gas motions broaden the line, lowering its optical depth and reducing this effect. Thus, resonant scattering can be used as a sensitive velocity diagnostic tool (for a review, see Churazov et al. 2010).

For galaxies with mean temperatures $\sim$0.3–1.0 keV, the Fe XVII 15.01 Å (optically thick), 17.05 Å and 17.1 Å (optically thin) lines are the most suitable for resonant scattering analyses, because their emissivity, along with the Fe XVII ionic fraction, peak in this temperature range (Fig. 1). By using the ratio of these lines, velocity amplitudes of the order of $\sim$100 km s^{-1} have been measured in the cores of three elliptical galaxies (Xu et al. 2002; Werner et al. 2009; de Plaa et al. 2012) and Perseus cluster (Churazov et al. 2004; Gastaldello & Molendi 2004).

In this work, we extend this resonant scattering analysis to a sample of 22 massive elliptical galaxies. We combine our resonant scattering measurements with independent line broadening results to obtain the best constraints to date on the turbulent velocity amplitudes, Mach numbers and non-thermal pressure contributions in giant elliptical galaxies, providing bounded constraints for 13 objects. This enables us, for the first time, to study common kinematic properties of the X-ray gas in elliptical galaxy cores.

The paper is organized as follows. We describe the *RGS* and *Chandra* data analysis in Section 2. The resonant scattering effect and simulations are described in Section 3. The results of the resonant scattering-only and resonant scattering-plus-line broadening analysis are presented in Section 4. Section 5 discusses the major assumptions and uncertainties in our study. We discuss our findings and their implications in Section 6 and provide conclusions in Section 7.

Throughout the paper, the abundance of heavy elements is given relative to the proto-solar abundances by Anders & Grevesse (1989).

2 OBSERVATIONS AND DATA ANALYSIS

2.1 Sample selection

The sources studied in this work constitute a sub-sample of the CHEmical Enrichment R*GS* cluster Sample (CHEERS) catalogue of X-ray bright galaxy groups, clusters and elliptical galaxies. Specifically, it includes galaxies with O VIII 19Å line detection (de Plaa & Mernier 2016; de Plaa 2017), plus two further cool galaxies with Fe XVII emission detected (NGC 1332 and IC 1459). From this initial group, we selected 22 objects in which the Fe XVII lines are detected. The properties of the sample are summarized in Table 1. The *XMM–Newton* observations are listed in Table 1 in Pinto et al. (2015), with addition of $\sim$120 ks of new data for IC 1459, awarded during *XMM–Newton* AO-14.

2.2 *RGS* data analysis

The *XMM–Newton* satellite is equipped with two main X-ray instruments: the *RGS* and *European Photon Imaging Camera* (*EPIC*). We have used the *RGS* data for our main spectral analysis and the *EPIC* (an MOS detector) data for imaging. The *RGS* spectrometers are slitless and the spectral lines are broadened by the source extent. As in Pinto et al. (2015), we corrected for spatial broadening through the use of *EPIC*-MOS surface brightness profiles, but used newer calibration files for data reduction and software versions (available from June 2016). We used the *XMM–Newton* Science Analysis System (SAS) v15.0.0, and corrected for contamination from soft-proton flares using the standard procedure described in Pinto et al. (2015).

For most objects, we adopted a slit (spectral extraction region) width of $\sim$0.8 arcmin ($\sim$5 kpc for most galaxies; cf. Table 3), providing good coverage of the inner Fe XVII bright core and maximizing the equivalent widths of the Fe XVII lines with respect to those produced by the hotter gas phase (see e.g. Pinto et al. 2016). For a few objects (NGC 4261, NGC 4374, NGC 4472 and NGC 5044) we extracted *RGS* spectra from regions maximizing the detection of resonant scattering (Section 6.4).

We subtracted a model background spectrum, using the standard *RGS* pipeline and a template background file based on the count rate in CCD 9. We produced MOS 1 images in the 8–27 Å wavelength band and extracted surface brightness profiles to model the *RGS* line spatial broadening with the relation: $\Delta\lambda = 0.138\ \Delta\theta$ Å (see the *XMM–Newton* Users Handbook).

2.2.1 *Baseline model*

Our analysis focused on the 8–27 Å first and second order *RGS* spectra. We performed the spectral analysis with SPEX version 3.00.00, using C-statistics and adopting 68 per cent errors.

For a full discussion on the spectral modelling, we refer the reader to Pinto et al. (2016). Briefly, we have described the ICM

Table 1. Properties of the sample of elliptical galaxies studied in this work.

Source	Alternative name	*Chandra* total exposure (ks)	*XMM–Newton* clean time (ks)	Distance[a] (Mpc)	Average temp. (keV)	Sound speed (km s^{-1})	$r_{\rm eff}^{b}$ (kpc)	$r_{\rm eff}$ reference[c]
IC 1459	–	60	156	21.1	0.70	430	3.5	B
NGC 507	–	44	95	65.5	1.19	560	1.7	D
NGC 533	A 189	40	35	137	0.93	500	14.5	M
NGC 708	A 262	140	173	69	1.32	590	11	S
NGC 1316	Fornax A	30	166	19	0.80	460	7.4	B
NGC 1332	–	60	64	19	0.80	460	9.2	R
NGC 1399	Fornax	130	124	19	1.00	520	32	Lo
NGC 1404	–	120	29	20	0.57	390	2.6	B
NGC 3411	NGC 3402	30	27	66.3	1.01	520	31	F
NGC 4261	–	100	135	29.4	0.68	450	5.7	T
NGC 4325	NGC 4368	30	22	108	0.86	480	14	L
NGC 4374	M 84	120	92	18.4	0.65	415	4.3	T
NGC 4406	M 86	30	64	16	0.81	460	7.9	B
NGC 4472	M 49	80	82	17.1	0.83	480	8.0	T
NGC 4552	M 89	200	29	15.3	0.58	390	2.3	T
NGC 4636	–	200	103	14.3	0.61	400	7.0	B
NGC 4649	M 60	310	130	17.3	0.87	480	6.5	T
NGC 4696	A 3526	760	153	44	1.14	550	82	Mi
NGC 4761	HCG 62	120	165	60	0.83	470	3.8	Sp
NGC 5044	–	70	127	38.9	0.82	480	10.4	T
NGC 5813	–	140	147	29.7	0.72	440	8.1	H
NGC 5846	–	170	195	26.3	0.63	410	9.8	H

Notes. [a]Adopted from Pinto et al. (2015) for consistency. [b]The effective radii used here are systematically smaller than the actual ones due to the way that they are measured, as discussed in depth by Kormendy et al. (2009). However, for our purpose of scaling the abundance profiles, such crude measurements are acceptable. [c]B–Bregman et al. (2005); D–Dullo & Graham (2014); F–Faber et al. (1989); H–Hu (2008); L–Laganá et al. (2015); Lo–Loubser et al. (2008); M–Ma et al. (2014); Mi–Misgeld, Hilker & Mieske (2009); R–Rusli et al. (2011); S–Saglia et al. (1997); Sp–Spavone et al. (2006); T–Temi, Mathews & Brighenti (2005).

emission with a model for an isothermal plasma in collisional ionization equilibrium (*cie*; ionization balance is adopted from Bryans, Landi & Savin 2009). The basis for this model is given by the MEKAL code (Kaastra, Mewe & Nieuwenhuijzen 1996), but several updates have been included (see the SPEX manual). The free parameters in the fits were the emission measures $Y = n_{\rm e}\, n_{\rm H}\, {\rm d}V$, temperature T and the abundances of N, O, Ne, Mg and Fe. The nickel abundance was fixed to that of iron. Most objects required two *cie* components to obtain an acceptable fit. In these cases, we coupled the abundances of the two *cie* components because the spectra do not allow us to measure them separately. The *cie* emission models were corrected for redshift, Galactic absorption and line-spatial-broadening through the multiplicative *lpro* component in SPEX, which uses as input the MOS 1 surface brightness profile (Section 2.2).

We did not explicitly model the cosmic X-ray background in the *RGS* spectra because any diffuse emission feature would be smeared out into a broad continuum-like component. For each source, we have simultaneously fitted the spectra of individual observations by adopting the same model. This gives a good description of the broad-band spectrum, but, as previously shown in Pinto et al. (2015), underestimates the 17 Å Fe XVII line peaks for several sources due to unaccounted for resonant scattering, which we model separately (cf. the following section). In Fig. 2, we show an example of a spectrum of NGC 4636.

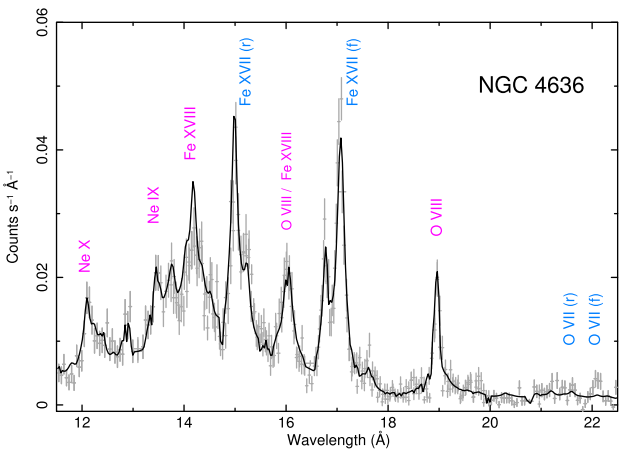

Figure 2. The *RGS* spectrum of NGC 4636 (OBS ID = 0111190701). Overlaid is a spectral model with two thermal components. The model underestimates both the O VII (22.1 Å) and Fe XVII (17.1 Å) forbidden lines and overestimates the Fe XVIII (14.2 Å) resonant line due to unaccounted resonant scattering effect.

2.2.2 *Fe XVII line measurements*

We have measured the fluxes of the Fe XVII resonant and forbidden lines by removing all lines associated with the Fe XVII ion from our plasma model (due to unaccounted for resonant scattering, cf. previous section) and fitting instead four delta lines broadened by the instrumental response fixed at 15.01 Å, 15.26 Å, 16.78 Å and 17.08 Å, which are the main Fe XVII transitions dominating the band considered. The lines were also corrected for redshift, galactic absorption and spatial broadening following the *cie* components.This method has been successfully used in previous papers (e.g. Werner et al. 2009, de Plaa et al. 2012, Pinto et al. 2016). From those fits we calculated the ratio of the Fe XVII forbidden to resonant lines for all sources. The results are shown in Table 3.

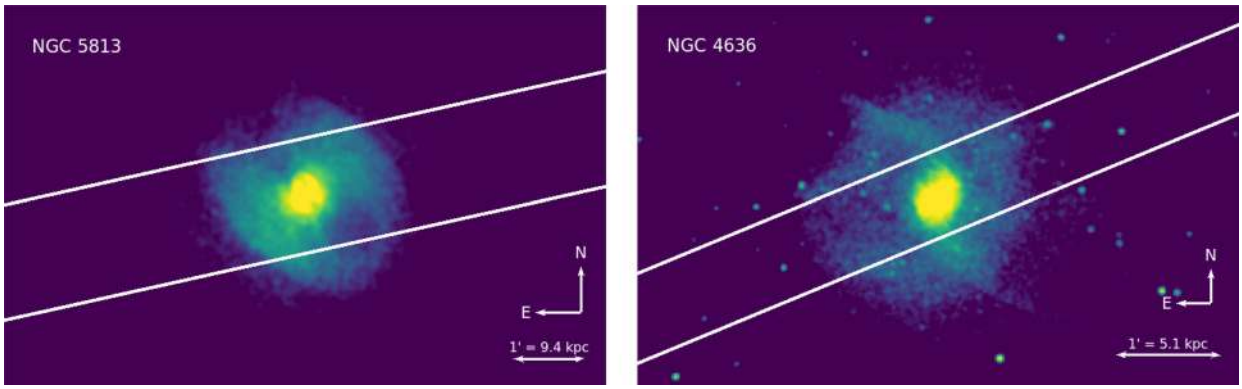

Figure 3. *Chandra* images of the elliptical galaxies NGC 5813 (left) and NGC 4636 (right) with the default *RGS* extraction regions overplotted (0.8 arcmin wide; Section 2.2). The images are lightly smoothed for visual purposes.

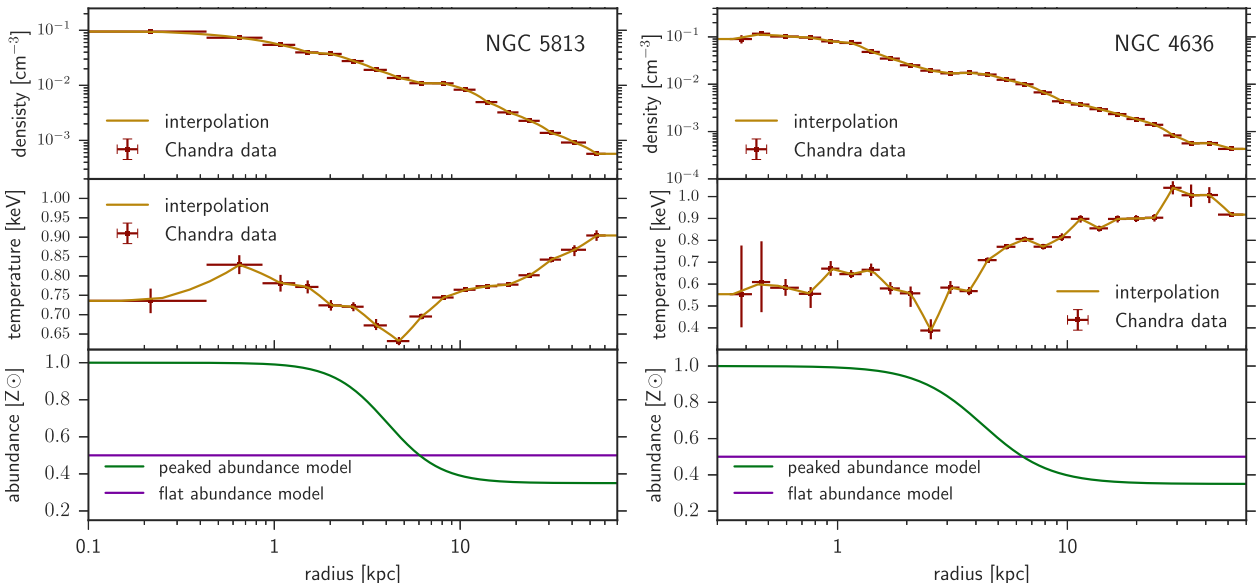

Figure 4. Thermodynamic properties of NGC 5813 (left) and NGC 4636 (right). Upper panels show the deprojected radial profiles derived from *Chandra* data (red points): number electron density (top) and gas temperature (centre), with 1σ error bars (Section 2.3); orange curves show the interpolated profiles used for radiative transfer simulations (Section 3.1). Bottom panels present abundance models adapted: fixed at 0.5 $Z_\odot$ (purple; default) and centrally peaked (green).

In Pinto et al. (2016), we showed that the low-temperature O VII and Fe XVII lines have widths narrower than the hotter O VIII and Fe XVIII lines. Therefore, in our fits, we have used two different *lpro* components: one *lpro* for the (hotter) *cie* component and the other *lpro* for the cooler O VII and Fe XVII delta lines. The scale parameters *s* of the two *lpro* components were uncoupled and free parameters in the fits.

2.2.3 *Line broadening analysis*

To provide further constraints on turbulence, we used in our analysis probability distributions on measured line widths using the method described by Pinto et al. (2015). Starting from our baseline model of two thermal *cie* components (Section 2.2.2), and using the *EPIC* surface brightness profiles, which provide an approximate spatial mapping for the lines in our spectra, we performed spectral fits and evaluated the C-statistics on a fixed velocity grid, with other parameters left free to vary. In particular, the *lpro* spatial scale factor $s = 0$–1 (i.e no spatial broadening and full *EPIC* broadening) was not fixed. This procedure is asymptotically equivalent to finding the marginalized velocity probability distribution.

2.3 *Chandra* data analysis

The initial data processing is done following the standard procedure described in Vikhlinin et al. (2005). The point sources are detected using the WVDECOMP tool and excluded from the analysis. Correcting for the exposure, vignetting effects and subtracting the background, images of the galaxies are produced (Fig. 3).

The deprojected number electron density and temperature are obtained from projected spectra using the procedure described in Churazov et al. (2003). The deprojected spectra are fitted with an isothermal APEC plasma model (Smith et al. 2001; Foster et al. 2012) in the 0.6–8 keV band using XSPEC (ver. 12.8.0). The fitted model takes into account the total galactic H I column density and assumes fixed constant abundance of heavy elements 0.5 $Z_\odot$. Examples of the deprojected profiles are shown in Fig. 4.

For several galaxies in our sample (NGC 708, NGC 1404, NGC 1399, NGC 4261, NGC 4406 and NGC 4472) we used published

deprojected radial profiles from Werner, Allen & Simionescu (2012). The deprojected data for NGC 4696 were provided by Sanders et al. (2016).

3 SIMULATIONS

For all objects in our sample, we conducted radiative transfer Monte Carlo simulations of the resonant scattering (Section 3.3). These simulations predict the fluxes of the 15.01, 17.05 and 17.1 Å Fe XVII lines, assuming different Mach numbers of turbulence, which are then compared to the measured flux ratios. We illustrate the analysis steps below using NGC 5813 and NGC 4636. Details for the rest of the objects are presented in the Appendix.

3.1 Input models

For our resonant scattering simulations, we adopted a spherically symmetric model of each galaxy based on the interpolated deprojected profiles of the gas electron number density and temperature (orange lines in Fig. 4; Section 2.3). In order to account for the uncertainty associated with 1σ errors in the deprojected data, we vary the models within plotted 68 per cent errors and repeat the calculations.

Since the abundance measurements of the heavy elements are uncertain, we performed simulations conservatively assuming a flat abundance profile fixed at 0.5 $Z_\odot$. The sensitivity of our results to the choice of the abundance model was checked by additionally considering a centrally peaked abundance profile, scaled by the galaxy's optical effective (half-light) radius $r_{\rm eff}$, namely:

$$Z_{\rm peaked}(r) = 0.65 \times \frac{2.0 + \left(\frac{r}{0.5 r_{\rm eff}}\right)^3}{1.0 + \left(\frac{r}{0.5 r_{\rm eff}}\right)^3} - 0.3 \quad [Z_\odot]. \tag{1}$$

In this case, the abundance is 1 $Z_\odot$ in the galaxy centre and drops to 0.35 $Z_\odot$ in the outskirts. Both models are shown in the bottom panels of Fig. 4. Effective radii used are listed in Table 1. As we discuss later, for most galaxies the choice of abundance model does not affect the results (Section 5.2).

3.2 Optical depth in the Fe XVII line

The optical depth τ of a galaxy in a given line is:

$$\tau = \int_0^\infty n_i \sigma_0 ds, \tag{2}$$

where s is the distance along the photon propagation, $n_{\rm i}$ is the number density of the ion in the ground state and σ_0 is the scattering cross-section at the centre of the line, given by:

$$\sigma_0 = \sqrt{\pi} h c r_e \frac{f}{\Delta E_D}. \tag{3}$$

Here, h is Planck constant, $r_{\rm e}$ is the classical electron radius, c is the speed of light, f is the oscillator strength of the respective atomic transition and $\Delta E_{\rm D}$ is the Doppler line width. $\Delta E_{\rm D}$ is given by:

$$\Delta E_D = \frac{E_0}{c}\left(\frac{2kT_e}{Am_p} + \frac{2}{3}V_{turb}^2\right)^{0.5}, \tag{4}$$

where E_0 is the rest frame energy of the atomic transition, k is the Boltzmann constant, A is the atomic mass number, $m_{\rm p}$ is the proton mass, $T_{\rm e}$ is the electron temperature and $V_{\rm turb}$ is the characteristic 3D turbulent velocity. We parametrize turbulence by the 3D Mach number,[1] $M = V_{\rm turb}/c_{\rm s}$, where $c_s = \sqrt{\gamma kT/(\mu m_p)}$ is the sound speed ($\gamma = 5/3$ is the adiabatic index for an ideal monoatomic gas and $\mu = 0.6$ is the mean particle atomic weight).

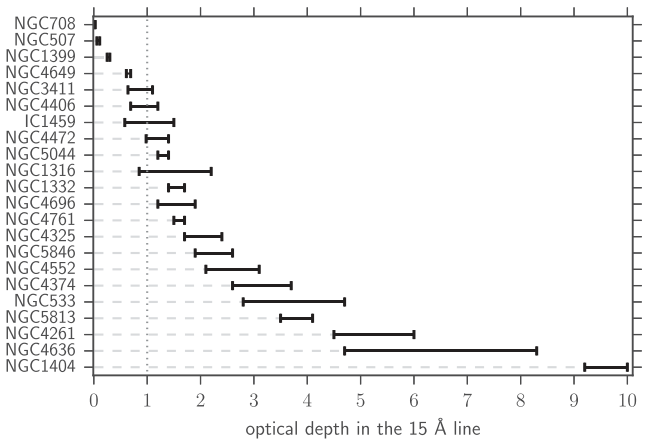

Figure 5. Optical depth (equation 2) in the optically thick Fe XVII line at 15.01 Å for all galaxies in our sample. Only thermal broadening is taken into account. The spread of each value reflects the 1σ uncertainty in the deprojected gas temperature and density profiles (see Section 3.1 and Fig. 4 for details). The dotted vertical line marks an optical depth of $\tau = 1$, beyond which line is considered optically thick. For the majority of galaxies in our sample the 15.01 Å Fe XVII line is optically thick. NGC 1404 has the largest optical depth due to its high density and low temperature, which results in a high Fe XVII ionic fraction.

Assuming no differential gas motions, the optical depths in the 15.01 Å line calculated for all galaxies in our sample are shown in Fig. 5. Most of the objects are optically thick in this line, and for almost a half of the sample $\tau > 2$. NGC 1404 has a very large optical depth of ~9–10, due to the combination of its large density and low temperature, resulting in a high ionic Fe XVII fraction. The other two lines considered in this study, 17.05 Å and 17.10 Å, are optically thin because of their low oscillator strengths (cf. Table 2).

3.3 Resonant scattering modelling

Our Monte Carlo simulations of resonant scattering follow the simulations performed by Sazonov, Churazov & Sunyaev (2002), Churazov et al. (2004) and Zhuravleva et al. (2010, 2011). Namely, we randomly draw the position and propagation direction of each photon (total number of photons $>10^7$), and draw its energy from a Doppler-broadened Gaussian around the line energy. Initially, we assign a unit weight to the photon, which is then reduced after each scattering event by a factor of 1-$e^{-\tau}$, until a minimal threshold ($\sim 10^{-9}$) is reached. Photons can undergo multiple scatterings before they leave the galaxy. After each event, a new position and propagation direction are drawn using a phase function, that is a sum of the isotropic and Rayleigh (dipole) scattering phase functions with appropriate weights (Hamilton 1947). We use ionization balance data and line emissivities from the APEC model for optically thin plasmas (Smith et al. 2001; Foster et al. 2012,

[1] In this work, we assume isotropic turbulence, i.e. $V_{turb} = \sqrt{3} v_{1D}$, where v_{1D} is the 1D differential velocity component. Our simulations assume fixed Mach number everywhere in the galaxy. Running simulations for fixed turbulent velocity instead changes our results by a maximum of 5 km s^{-1} in only one galaxy.

Table 2. Properties of the Fe XVII line transitions considered in this work, adopted from AtomDB data base ver. 2.0.2.

Wavelength (Å)	Energy (keV)	Lower level	Upper level	Oscillator strength	Electron configuration lower	Electron configuration upper	Transition type	Rayleigh scattering weight, w_R
15.01	0.826	1	27	2.49	$2p^6$, ^1S, J = 0	$2p^5$ 3d, ^1P, J = 1	Electric dipole	1
17.05	0.727	1	3	0.126	$2p^6$, ^1S, J = 0	$2p^5$ 3s, $^2P_{3/2}$, J = 1	Electric dipole	1
17.10	0.725	1	2	5.2×10^{-8}	$2p^6$, ^1S, J = 0	$2p^5$ 3s, $^2P_{3/2}$, J = 2	Magnetic quadrupole	–

Table 3. Constraints on turbulence in our sample of elliptical galaxies, divided into subgroups according to the availability of the resonant scattering limit derived (Section 4.1) and method used. RS: resonant scattering-only probability distributions (Section 4.1); RS+LB: resonant scattering-plus-line broadening probability distributions (Section 4.2). Results are shown for: M – 3D Mach number, v_{1D} – line-of-sight turbulent velocity amplitude and $\epsilon_{turb}/\epsilon_{th}$ – turbulent to thermal pressure fraction. The *RGS* measured flux ratio with 1σ statistical uncertainty, along with the physical size of the *RGS* extraction region (the slit width; cf. Fig. 3) are also provided. Note that these measurements are performed using our fiducial model. We discuss in detail the effects of systematic uncertainties and model assumptions in Section 5.

Source name	*RGS* slit width (kpc)	Measured flux ratio	RS-only 1σ/68 per cent limits M	RS-only 1σ/68 per cent limits v_{1D} (km s^{-1})	RS+LB 1σ/68 per cent limits M	RS+LB 1σ/68 per cent limits v_{1D} (km s^{-1})	RS+LB 1σ/68 per cent limits $\epsilon_{turb}/\epsilon_{th}$ (per cent)
			I. Bounded constraints				
NGC 4636	4.0	1.95 ± 0.09	$0.52^{+0.22}_{-0.22}$	121^{+51}_{-35}	$0.52^{+0.22}_{-0.15}$	121^{+51}_{-36}	12^{+15}_{-7}
NGC 5813	7.4	1.8 ± 0.1	$0.44^{+0.21}_{-0.12}$	111^{+54}_{-31}	$0.37^{+0.12}_{-0.09}$	94^{+29}_{-24}	$6.3^{+5.9}_{-2.7}$
			II. Upper limits				
NGC 1316	4.4	1.8 ± 0.1	$0.23^{+0.24}_{-0.23}$	61^{+63}_{-61}	<0.28	<73	<5.1
NGC 4374	3.2	2.1 ± 0.2	$0^{+0.26}_{-0}$	0^{+63}_{-0}	$0^{+0.19}_{-0}$	0^{+47}_{-0}	<3.2
			III. Lower limits				
NGC 1404	4.6	2.0 ± 0.2	>0.46	>103	$1.02^{+0.58}_{-0.39}$	230^{+130}_{-90}	35^{+38}_{-18}
NGC 3411	15	1.1 ± 0.3	>0.15	>46	$0.58^{+0.66}_{-0.38}$	170^{+200}_{-110}	<43
NGC 4261	1.1	1.9 ± 0.5	>0.079	>19	$0.29^{+0.43}_{-0.23}$	71^{+105}_{-57}	<24
NGC 4325	25	1.4 ± 0.6	>0.12	>34	$0.86^{+0.83}_{-0.57}$	240^{+230}_{-160}	<52
NGC 4552	3.6	1.6 ± 0.3	>0.22	>49	$0.79^{+1.31}_{-0.49}$	180^{+290}_{-110}	8^{+46}_{-8}
NGC 4649	4.0	1.3 ± 0.2	>0.081	>23	$0.26^{+0.32}_{-0.19}$	71^{+91}_{-51}	<16
NGC 4761	14	1.3 ± 0.1	>0.23	>62	$0.61^{+0.41}_{-0.33}$	166^{+114}_{-90}	<39
NGC 5044	9.6	1.3 ± 0.1	>0.30	>83	$0.61^{+0.39}_{-0.28}$	172^{+108}_{-79}	8^{+35}_{-6}
NGC 5846	7.4	1.7 ± 0.2	>0.24	>56	$0.32^{+0.25}_{-0.14}$	77^{+58}_{-34}	3^{+12}_{-3}

IV and V. No resonant scattering limit

Source name	*RGS* slit width (kpc)	Measured flux ratio	Reason behind the lack of limit
NGC 1332	4.4	2.7 ± 0.8	qualitative description (see Section 4.1.IV); additional data necessary
NGC 4406	3.8	2.1 ± 0.3	
NGC 4472	1.5	2.2 ± 0.3	
NGC 507	15	1.0 ± 0.4	low concentration of Fe XVII ions
NGC 708	16	1.4 ± 0.2	
IC 1459	5.0	1.7 ± 0.5	very large scatter on measured line ratios; for further improvements additional data necessary
NGC 533	32	2.1 ± 0.7	
NGC 1399	4.4	1.3 ± 0.2	
NGC 4696	10	1.5 ± 0.1	

AtomDB ver. 2.0.2[2]). Line transition properties and dipole scattering weights are listed in Table 2.

3.4 Calculating the Fe XVII line flux ratio

Our Monte Carlo simulations provide projected line fluxes I_M as a function of projected radius r_p, given a specific 3D Mach number M. These profiles take into account resonant scattering, along with thermal and turbulent line broadening. The primary quantity of interest is the projected flux ratio (FR) of optically thin (17.05 Å, 17.10 Å) to thick (15.01 Å) Fe XVII lines (the 17.05 Å and 17.10 Å lines are observationally indistinguishable, thus their sum is considered). For each object in our sample, we predicted the projected radial profiles of FR varying levels of turbulence (parametrized by the Mach number M):

$$FR(r_p, M) = \frac{I_{17.05[\text{Å}]}(r_p, M) + I_{17.10[\text{Å}]}(r_p, M)}{I_{15.01[\text{Å}]}(r_p, M)}. \quad (5)$$

An example is shown in Fig. 6.

[2] http://www.atomdb.org/

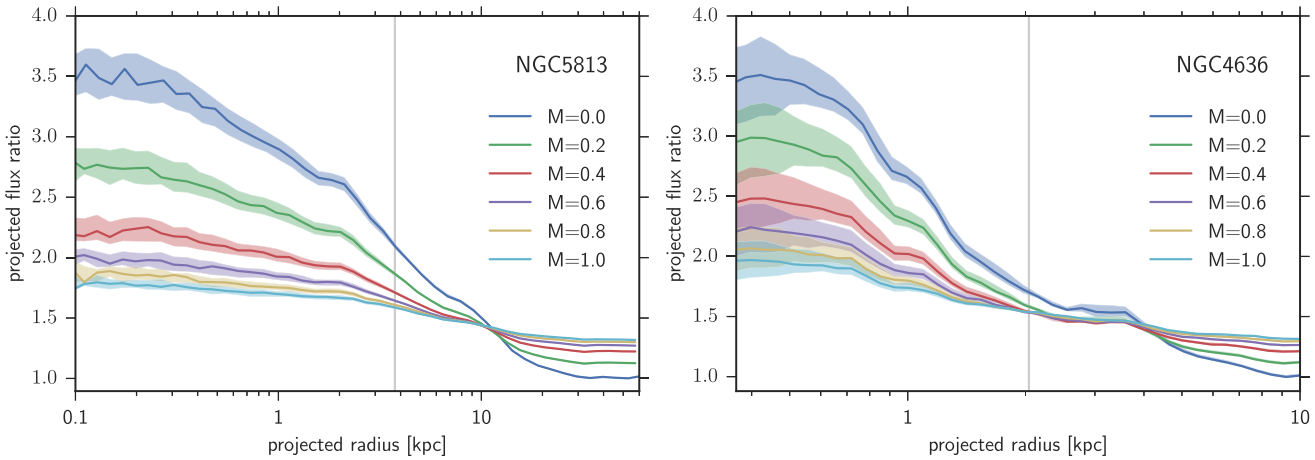

Figure 6. Predicted projected radial profiles of the Fe XVII optically thin to thick line flux ratio (equation 5) in NGC 5813 (left) and NGC 4636 (right), calculated assuming isotropic turbulence with different 3D Mach numbers M, with the uncertainty associated with the 1σ errors in the deprojected temperature and density profiles (Section 3.1 and Fig. 4). Grey vertical line marks the size of the spectral extraction region (Fig. 3 and Section 2.2). The lower the Mach number, the stronger the suppression of the Fe XVII optically thick line. This trend reverses at larger radii, where the line becomes optically thin (see Section 6.4), which happens at ∼10 kpc in NGC 5813 and at ∼4 kpc in NGC 4636.

The observed flux ratio comes from a spatially extended *RGS* spectral extraction region (shown in Fig. 3). We numerically integrate line fluxes over this region A (a 0.8 arcmin wide slab[3]):

$$IFR(M) = \frac{\int_{slab}(I_{17.05[\text{Å}]}(r_p, M) + I_{17.10[\text{Å}]}(r_p, M))dA}{\int_{slab} I_{15.01[\text{Å}]}(r_p, M)dA}. \quad (6)$$

These integrated flux ratios (IFRs) are then compared to observations, as illustrated in Fig. 7.

4 RESULTS

We present two sets of results: first, based on resonant scattering effect only and secondly, using combined resonant scattering and line broadening methods. In the main text, we present detailed results for NGC 4636 and NGC 5813. The rest of the sample is shown in Fig. A1.[4] Results are summarized in Table 3.

4.1 Resonant scattering-only

We first compare our observations (red line and region in Fig. 7) to our fiducial model for the integrated flux ratio, namely simulations run for a flat abundance profile and deprojected thermodynamic profiles without uncertainties (blue line in Fig. 7). This follows the approach of previous resonant scattering works, e.g. Werner et al. (2009) and de Plaa et al. (2012). Lower limits for eight galaxies can be derived this way,[5] on average showing $M > 0.59$ ($v_{1D} > 133\,\mathrm{km\,s^{-1}}$). NGC 4261 has the lowest lower limit on Mach number, $M > 0.054$ ($v_{1D} > 13\,\mathrm{km\,s^{-1}}$), while NGC 1404 shows the largest lower limit, $M > 0.59$ ($v_{1D} > 130\,\mathrm{km\,s^{-1}}$). For the remainder of the sample, we cannot obtain any limits using this approach.

[3] For some objects (NGC 4261, NGC 4374, NGC 4472 and NGC 5044), we actually use narrower slits to maximize the resonant scattering signal (Section 6.4).

[4] We show all galaxies for which the effect of resonant scattering is important.

[5] M89, NGC 1404, NGC 4261, NGC 4325, NGC 4636, NGC 4649, NGC 5813 and NGC 5846.

In order to extract our formal constraints on the Mach number, we approximated the uncertainties on the predicted IFR (blue regions in Fig. 7) as Gaussians. We then convolved this uncertainty with the statistical error on the observed ratio and calculated the probability density function (pdf) of a Mach number. The normalized pdfs are shown with black curves in Figs 7 and A1. The peaks of the pdfs are indicated with the vertical dashed lines, where appropriate (in seven galaxies). Note that in most cases the peaks coincide with the intersection of the blue (simulated ratio for fiducial model) and the red (measured ratio) curves.

Assuming that the turbulence in galaxies is subsonic, i.e. $M < 1$, confidence intervals are obtained from the pdfs. Green regions in Fig. 7 show the 68 per cent confidence intervals, providing constraints of $M = 0.44^{+0.21}_{-0.12}$ ($v_{1D} = 111^{+54}_{-31}\,\mathrm{km\,s^{-1}}$) in NGC 5813 and $M = 0.52^{+0.22}_{-0.15}$ ($v_{1D} = 121^{+51}_{-35}\,\mathrm{km\,s^{-1}}$) in NGC 4636. We obtain well-bounded constraints and upper or lower limits for 11 other systems: NGC 1316, NGC 1404, NGC 3411, NGC 4261, NGC 4325, NGC 4374, NGC 4552, NGC 4649, NGC 4761, NGC 5044 and NGC 5846. For three galaxies, the pdfs show a preference for lower Mach numbers, but are too flat to derive meaningful upper limits; for six galaxies the distributions are completely flat, thus we cannot constrain turbulent velocities in these objects with resonant scattering. For some of these galaxies, it would be straightforward to obtain a resonant scattering measurement, provided more data (Section 6.4).

Below we summarize the derived constraints, listed in Table 3, by dividing galaxies into five groups. Summary plot for groups I–III is shown in Fig. 8 (left), with group I shown in blue, group II in purple and group III in black. The sensitivity of the results to the assumed maximum Mach number $M_{\max} = 1$ (the prior) is discussed in Section 5.5.

I. Peaked distributions: bounded constraints. Two galaxies, NGC 4636 and NGC 5813, show clearly peaked distributions that allow us to report the most probable value with 68 per cent confidence (lower and upper limits; Fig. 7). Changing the Mach number prior does not affect the results significantly.

II. Peaked distributions: low turbulence. Two more objects have clearly peaked distributions: NGC 4374 and NGC 1316 (Fig. A1). Both galaxies have low turbulence, and the confidence intervals do

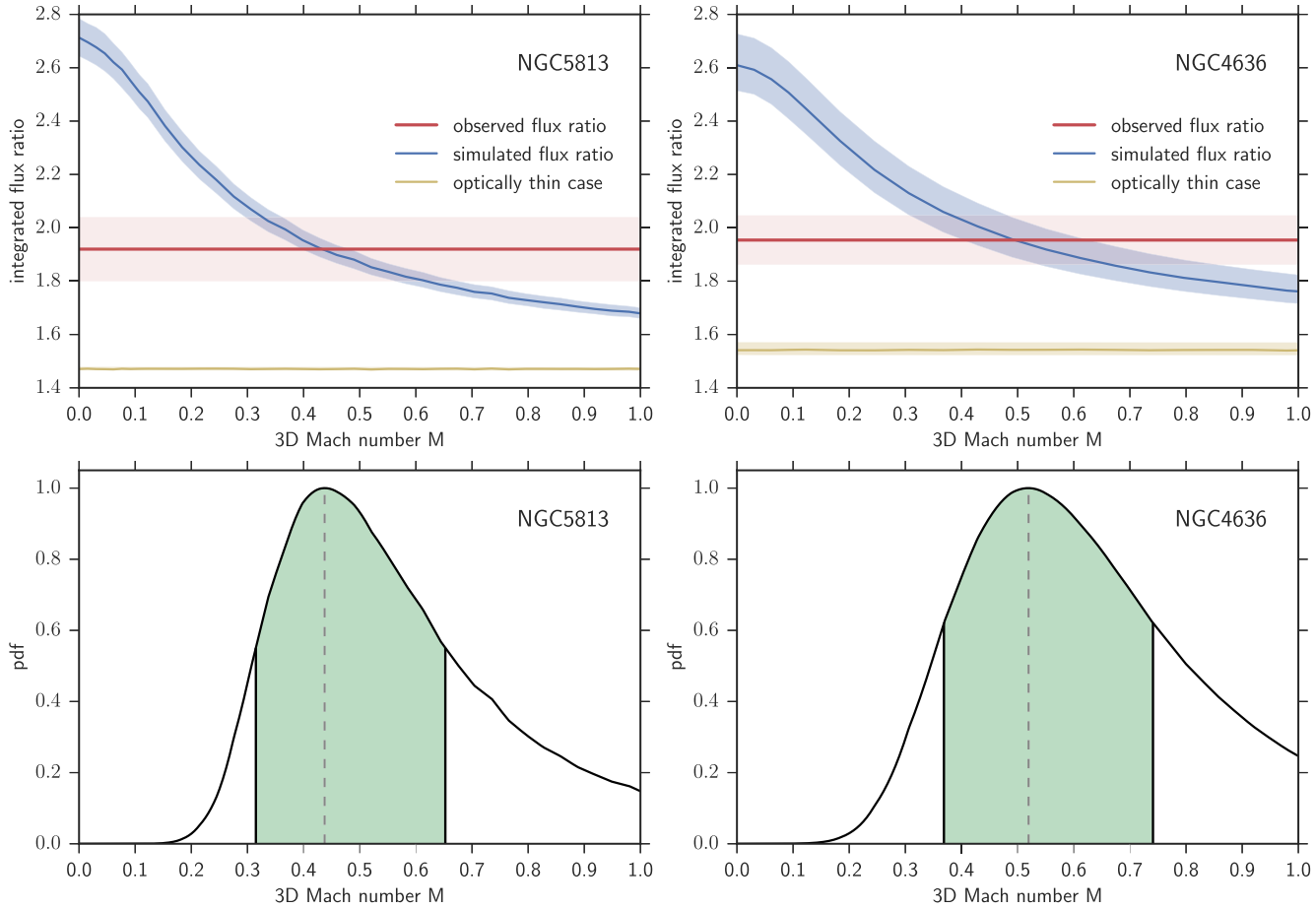

Figure 7. Resonant scattering results. Upper panels: comparison of the observed and simulated flux ratio predicted for different turbulent motions for NGC 5813 (left) and NGC 4636 (right; Section 3.4). The red line and region show the flux ratio measured from *RGS* observations (plus 68 per cent uncertainties). The blue line and region show predicted integrated flux ratio as a function of 3D Mach number M (equation 6) with the uncertainty associated with 1σ errors in the deprojected thermodynamic profiles (Section 2.3). The optically thin limit is shown in yellow. The two regions overlap for Mach numbers $M \sim 0.30$–0.67 in NGC 5813, and for $M \sim 0.30$–0.85 in NGC 4636, providing constraints on turbulence. Lower panels: unnormalized probability density function of Mach number in NGC 5813 (left) and NGC 4636 (right; Section 4.1). Dashed vertical line marks the most probable Mach number: 0.44 in NGC 5813 and 0.52 in NGC 4636. Green regions represent the 1σ confidence intervals: $M = 0.32 - 0.65$ for NGC 5813 and $M = 0.37$–0.74 for NGC 4636, which translate to $v_{1D} = 111^{+54}_{-31}$ km s^{-1} and $v_{1D} = 121^{+51}_{-35}$ km s^{-1}, respectively.

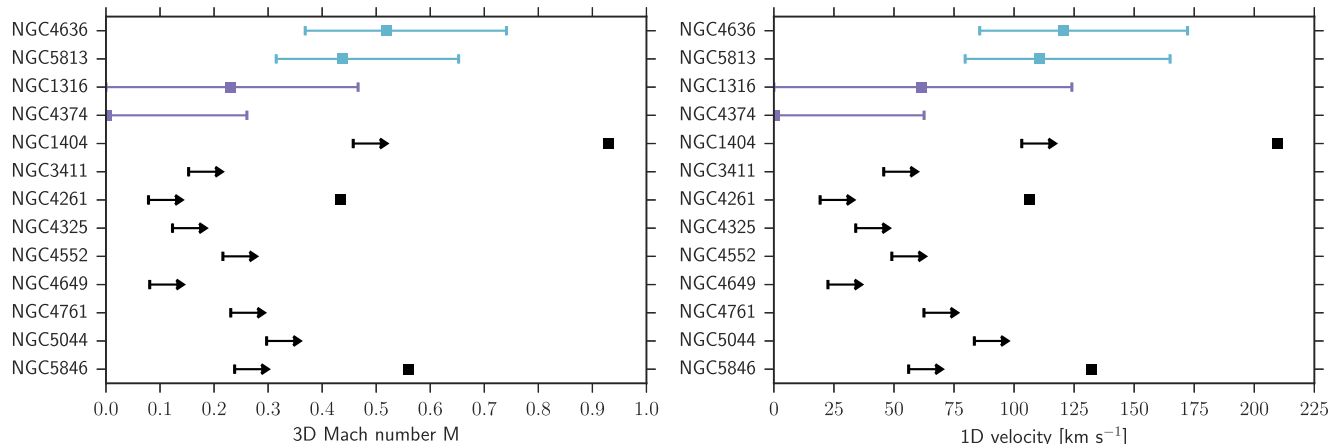

Figure 8. Resonant scattering constraints on 3D Mach number (left-hand panel) and 1D turbulent velocity amplitude (right-hand panel) for galaxies in our sample. Blue and purple points show 1σ limits for galaxies in groups I and II, while black show 2σ upper limits of group III objects (full pdfs are shown in Figs 7 and A1; see Section 4.1 for details). Squares mark the most probable value (where available).

not provide meaningful lower limits. However, since the only difference between the former and latter groups is that the distributions are shifted towards smaller Mach numbers, we treat them the same way as galaxies in group I and report the most probable value with a 68 per cent upper limit and a lower limit of 0.

III. Lower limits. Resonant scattering technique is better suited for providing lower rather than upper limits on gas motion velocities: the stronger the turbulence, the smaller the line suppression (Section 3.2). Therefore, the integrated flux ratio in the case of large Mach numbers approaches the constant optically thin plasma case (cf. the blue and yellow lines in Fig. 7). Since pdfs flatten at large M (cf. Fig. A1), our velocity constraints depend on maximum Mach number $M_{\rm max}$ assumed. We note that lower limits are least sensitive to the choice of Mach number prior (Section 5.5).

For the majority of the objects in our sample (9; see Table 3) we are able to provide lower limits only (at 95 per cent confidence intervals; for pdfs see Fig. A1). Among these objects, three galaxies also show the most probable value (NGC 1404, NGC 4261 and NGC 5846). The mean lower limit is 0.178 (47 km s^{-1}), excluding NGC 1404, which is an obvious outlier (lower limits: $M > 0.46$, $v_{\rm 1D} > 103$ km s^{-1}).

IV. Low turbulence – qualitative description. Three galaxies, NGC 1332, NGC 4406 and NGC 4472, have high observed flux ratios, indicating that the optically thick line is suppressed due to resonant scattering. This points towards low turbulence, which is reflected in the pdfs of these objects (Fig. A1). The effect itself is not strong, and the resulting probability distributions are too flat for deriving limits. However, we can see that the pdf at $M = 0$ is approximately ∼5 times more than at $M = 0.5$ or $M = 1$ in NGC 4406, ∼3 times more likely in NGC 4472 and ∼2 times more likely in NGC 1332.

V. No limits. For six galaxies, we are not able to derive any turbulence constraints. NGC 708 and NGC 507 have the largest gas temperatures in our sample and the resonant Fe XVII line is optically thin. Other objects (e.g. NGC 1399, NGC 4696) are more distant, thus their innermost regions, where most of the scattering occurs, have angular sizes significantly smaller than the *RGS* aperture used. Current *RGS* data does not allow us to measure line ratios reliably in such regions (Section 6.4).

The characteristic line-of-sight one-component turbulent velocity amplitude $v_{\rm 1D}$ can be derived directly from the 3D Mach number. If turbulence is isotropic, then:

$$v_{\rm 1D} = \frac{1}{\sqrt{3}} M c_s = \frac{1}{\sqrt{3}} M \sqrt{\frac{\gamma k T_e}{\mu m_p}}. \quad (7)$$

The temperature $T_{\rm e}$ that we use here is the mass weighted average electron temperature calculated within the spectral extraction region from the deprojected temperature profile. The temperatures of galaxies, along with respective sound speeds, are shown in Fig. 9 and Table 1. The derived turbulent velocity constraints are listed in Table 3, and shown in the right-hand panel of Fig. 8. Typical lower limits are 20–60 km s^{-1}. For a few objects the measured velocities are between 43–121 km s^{-1}.

4.2 Resonant scattering-plus-line broadening

The velocity dispersion of the X-ray emitting gas can be measured directly through line broadening. Since the *RGS* is a slitless spectrometer, the spatial extent of the galaxy core broadens the lines in addition to natural, thermal and turbulent broadening. Therefore, direct velocity measurements provide mostly upper limits (e.g. Pinto et al. 2015, and Section 2.2). We obtained the line broadening velocity probability distributions by performing spectral fitting, varying the velocity and evaluating the C-statistics each time (Section 2.2.3). These pdfs are then combined by multiplying with the pdfs from the resonant scattering analysis (Section 4.1).

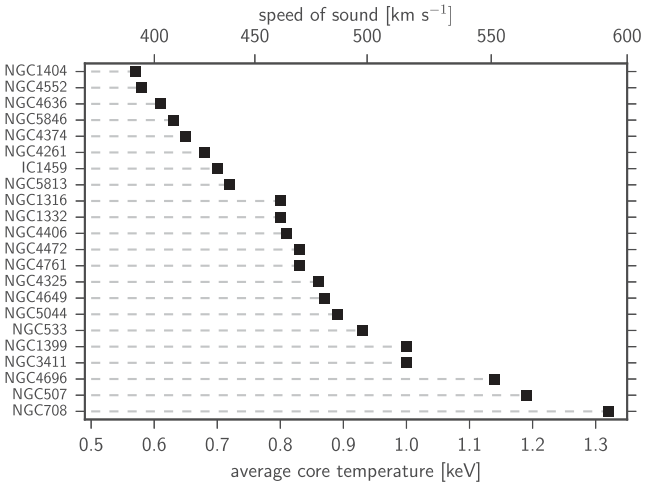

Figure 9. Average temperature within the *RGS* extraction region (bottom axis) and respective sound speed (top axis; this axis has a square root scaling) calculated for all galaxies in our sample.

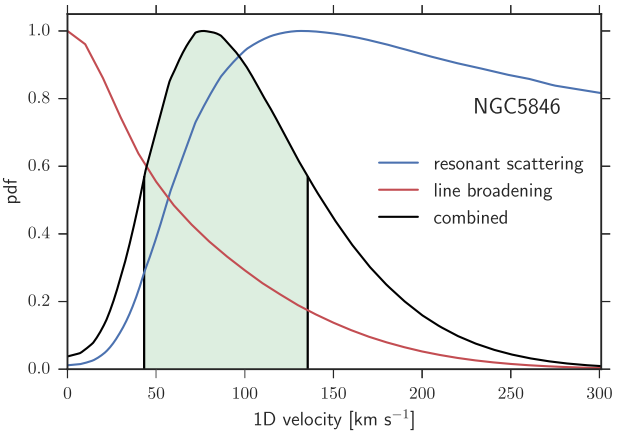

Figure 10. Combined resonant scattering and line broadening measurement in NGC 5846. By using respective probability distributions (blue and red lines), a combined distribution is obtained (black line), which allows us to derive the most probable velocity with 1σ lower and upper limits (green region). For details, see Section 4.2.

Fig. 10 illustrates the result of this procedure for NGC 5846. The blue line shows the resonant scattering pdf, which provides only a lower limit on the velocity, while the red line shows the line broadening pdf, which gives only an upper limit. The combined distribution, shown in black, is peaked and narrow, and provides a velocity measurement with 68 per cent uncertainties (green region). Analogous plots for the remaining galaxies can be found in Fig. 11.

4.3 Exploring the sample properties

Using the combined distributions we are able to *measure* velocities of gas motions in 13 galaxies in our sample. We have examined the distribution of measured velocity values, which, in principle, can

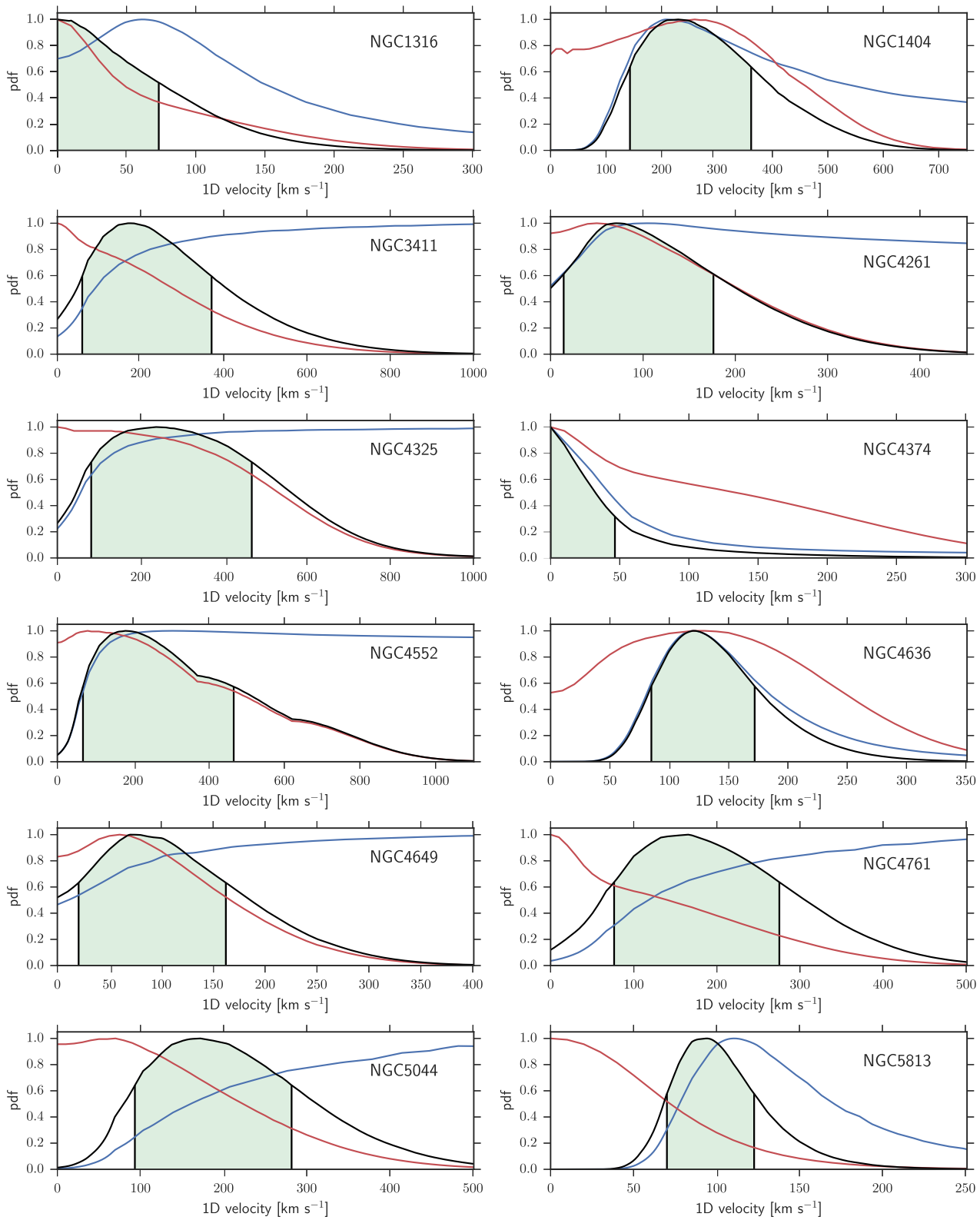

Figure 11. Combined resonant scattering (blue) and line broadening (red) probability distributions as a function of one-component velocity (black), with 1σ confidence regions (green), shown for the remainder of the sample. Derived constraints are listed in Table 3. See Section 4.2 for details.

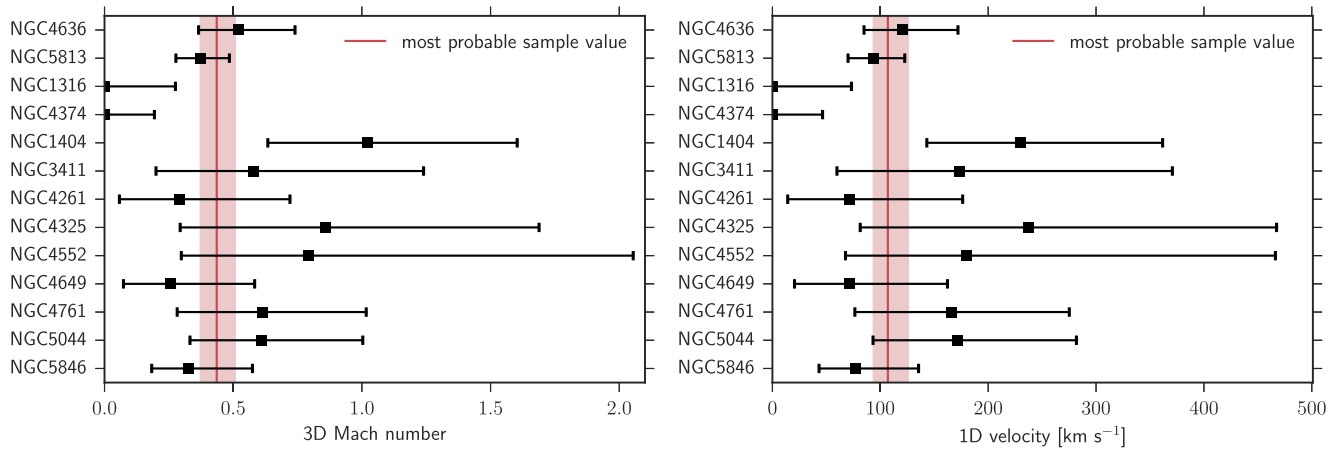

Figure 12. Combined resonant scattering and line broadening constraints on 3D Mach number (left-hand panel) and 1D turbulent velocity amplitude (right-hand panel) for galaxies in our sample, with 1σ uncertainties. Red lines and regions show best fit most probable sample values fitted to the measurements, $M_{mp} = 0.44^{+0.07}_{-0.06}$ for Mach number and $v_{1D,mp} = 107^{+19}_{-15}$ km s^{-1} for velocity. In both cases, the data shows scatter around most likely values to be consistent with zero within current uncertainties.

provide key information on e.g. processes that are responsible for the motions. A summary plot is shown in Fig. 12 (see also Table 3).

We fit the measured velocities and Mach numbers with single mean values, allowing for scatter, using Monte Carlo Markov Chain method. The resulting most probable values are $v_{1D,mp} = 107^{+19}_{-15}$ km s^{-1} and $M_{mp} = 0.44^{+0.07}_{-0.06}$ (shown with red lines and regions in Fig. 12). In the case of both the velocity and Mach number, the scatter is consistent with zero with 1σ upper limits of 38 km s^{-1} and 0.16, respectively.

Note that by utilizing the line broadening pdfs, which provide upper limits, we derive these measurements with no prior maximum Mach number assumption, as opposed to the pure resonant scattering case (cf. Section 4.1).

4.4 Turbulent pressure

Knowing the characteristic Mach number, we can place constraints on the non-thermal pressure contributed by turbulence. The energy density of turbulence $\epsilon_{\rm turb}$ is given by:

$$\epsilon_{turb} = \frac{3}{2}\varrho v_{1D}^2 = \frac{1}{2}\varrho c_s^2 M^2, \quad (8)$$

where ϱ is the gas mass density. On the other hand, the thermal energy density is:

$$\epsilon_{th} = \frac{3}{2}\frac{\varrho kT}{\mu m_p}. \quad (9)$$

The fraction of the turbulent non-thermal to thermal pressure is a ratio of the two energy densities:

$$\frac{\epsilon_{turb}}{\epsilon_{th}} = \frac{\gamma}{3}M^2. \quad (10)$$

In order to measure the turbulent pressure support we used the combined resonant scattering and line broadening probability distributions of Mach numbers (Section 4.2) and calculated respective pressure distributions. In Fig. 13, we show the resulting 68 per cent constraints on pressure support (listed in Table 3). The data are consistent with no scatter around a single constant value of $5.6^{+2.6}_{-1.5}$ per cent, shown with a red line in Fig. 13. The 1σ upper limit on scatter is 2.6 per cent.

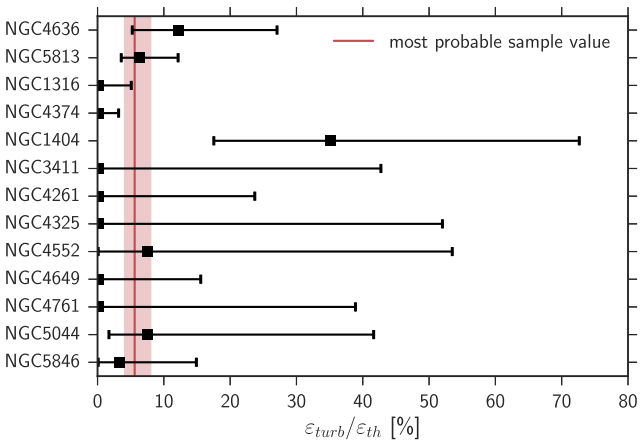

Figure 13. Turbulent pressure support in sample galaxies (Section 4.4), with 1σ uncertainties based on combined resonant scattering and line broadening pdfs (Section 4.2). Red line and region show the best-fitting constant: $5.6^{+2.6}_{-1.5}$ per cent. Within current uncertainties, the data does not show any scatter around this single value.

5 SYSTEMATIC UNCERTAINTIES

Our resonant scattering analysis makes a number of simplifying assumptions. First, we assumed spherically symmetric models of galaxies, which is a crude approximation given that the morphology of some objects is quite disturbed (e.g. filamentary structure, bubbles etc.; see Section 6.4 for possible future improvements). Secondly, we fitted the deprojected spectra at a given radii with a single temperature model. This might introduce a bias, since the Fe XVII line emissivity and ionic fraction are strong functions of temperature (Fig. 1). For some galaxies there is no evidence that a multiphase gas exists in a volume-filling way in their cores (e.g. in NGC 5044 and NGC 5813, de Plaa et al. 2012), while for others it is likely the case (e.g. in NGC 4696, Sanders et al. 2016). Finally, we have only considered isotropic turbulent motions, characterized by a single Mach number. If instead motions are anisotropic, the amplitude of line suppression due to scattering will change. Namely, if motions are predominantly in the radial direction, then for a given velocity amplitude the line suppression will be smaller than in the case of isotropic motions (Zhuravleva

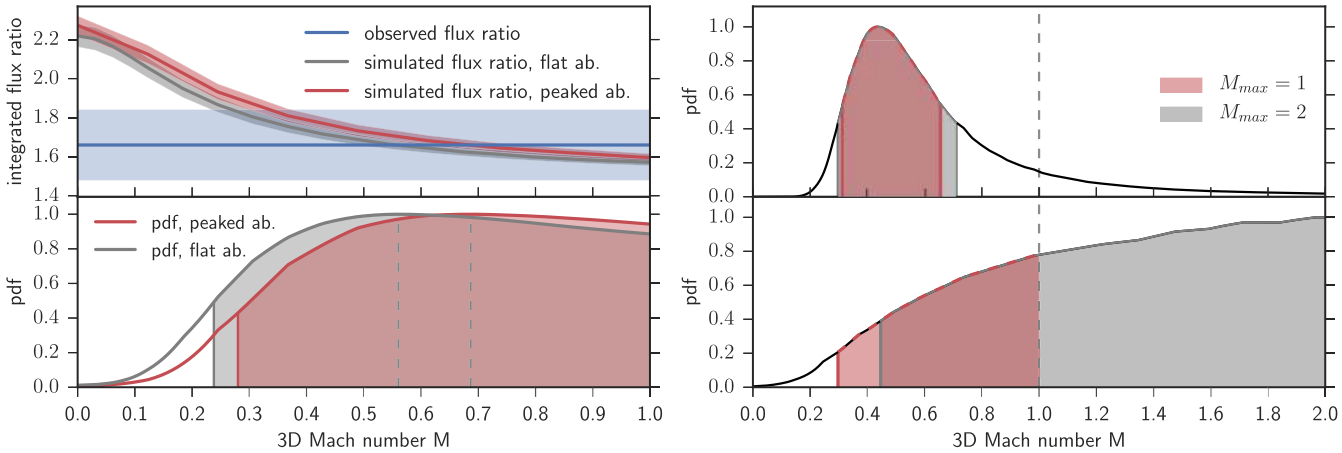

Figure 14. Left: results for NGC 5846, assuming flat (grey; default) and peaked abundance models (red; Section 3.1). Upper panel is the same as Fig. 7, and lower panel is the same as Fig 7. Lower limit derived with peaked abundance model is larger by 18 per cent (10 km s^{-1}), and the most probable value is larger by 23 per cent (29 km s^{-1}) than values inferred with flat abundance model (Section 5.2). Right: dependence of derived constraints on the maximum Mach number: the default case $M_{\rm max} = 1$ (grey dashed line) and $M_{\rm max} = 2$ case correspond to the red and grey confidence intervals, respectively. Upper panel shows 1σ limits in a peaked probability distribution in NGC 5813, where the lower limit changes from 0.32 to 0.3 (by 4 km s^{-1}), and the upper changes from 0.65 to 0.71 (by 12 km s^{-1}). Lower panel shows 2σ limits in a non-peaked distribution in NGC 5044, where the lower limit changes from 0.3 to 0.45 (by 34 km s^{-1}). See Section 5.5 for discussion.

et al. 2011). Measuring anisotropy effects will require spatial mapping with future microcalorimeter-like high spectral resolution data (Section 6.5).

Other key major systematic uncertainties are associated with the line spread function of *RGS*, the abundance of heavy elements, current atomic data, charge exchange, and the choice of the maximal Mach number. We explore each of these in turn.

5.1 *RGS* instrumental uncertainty

The Line Spread Function of the *RGS* is known with accuracy of 5–10 per cent, making the instrument less sensitive to low-velocity line broadening. This uncertainty has a small effect on the measured line flux ratios. Therefore, it does not affect the majority of our results, since most pdfs at low velocities are dominated by the resonant scattering measurement, which relies on the observed line flux ratios.

There are two exceptions: NGC 1316 and NGC 4374, where the line broadening pdf is important at low velocities. However, in these two galaxies the resonant scattering and line broadening independently provide similar constraints. If line broadening was not included, the upper limits on velocities would rise by $\sim$50 km s^{-1} in NGC 1316 and $\sim$15 km s^{-1} in NGC 4374 (cf. Table 3). Larger uncertainties in these galaxies would reduce the limit on the scatter around the common sample velocity, leaving the best-fitting sample velocity unchanged. Therefore, this effect does not affect our conclusions.

5.2 Abundance of heavy elements

Obtaining robust abundance measurements for elliptical galaxies from current X-ray spectra is challenging. Thus, we conservatively choose to use a flat abundance, fixed at 0.5 Z$_\odot$, as our default model. This value is consistent with recent average iron abundance profile for group central galaxies in the CHEERS sample (Mernier et al. 2017).

In order to test sensitivity of our measurements to this assumption, we repeated the calculations assuming a peaked abundance model (equation 1, Section 3.1 and Fig. 4). For most galaxies, the results weakly depend only on the adopted profile, with the difference $<$20 per cent. We illustrate this in NGC 5846 (Fig. 14, left-hand panel), in which the lower limit on Mach number is increased by 18 per cent (10 km s^{-1}), and the most probable value by 23 per cent (29 km s^{-1}) if the peaked abundance model is assumed instead of the constant value of 0.5 Z$_\odot$. This is smaller than a nominal 68 per cent uncertainty almost by a factor of 2.

A few objects show substantial differences, $\sim$20–50 per cent (40–50 km s^{-1}; NGC 1404, NGC 4261, NGC 4552 and NGC 4636). In these galaxies, the physical size of the spectral extraction region is small compared to the half-light radius used to scale the peaked abundance profile, meaning that effectively the profile is flat within the extraction region with a value double the one adopted in the default flat model. This doubles the amount of Fe XVII ions present in the gas, leading to larger optical depths in considered lines (e.g. τ changing from $\sim$6 to $\sim$12 in NGC 4636), which results in more efficient resonant scattering and slightly different constraints than in the default case.

We note that abundance profiles with a central drop are sometimes observed in elliptical galaxies (e.g. Panagoulia, Sanders & Fabian 2015). However, this drop might be a result of fitting a simplified model to a multiphase gas in the galactic core (e.g. Buote et al. 2003). Therefore, we do not consider a model with a central drop in this work.

5.3 Atomic data

The Fe XVII ion used in our analysis provides critical spectral diagnostics. However, due to the complicated inner structure of the ion, complete agreement between experimental results and theoretical predictions of the atomic properties has not yet been reached (but is expected to be achieved when high order effects are included in calculations, e.g. Brown et al. 2006).

The two major current astrophysical plasma codes, APEC and SPEX, predict slightly different optically thin ratios of the lines considered in this work, e.g. for a 0.6 keV plasma, the ratio $\sim$1.5 is predicted by APEC and $\sim$1.3 by SPEX. Here, we use APEC ver. 2.0.2 for our fiducial

models,[6] because the respective atomic properties of Fe XVII are closer to the experimental measurements from EBIT and LCLS (Brown et al. 2001; Bernitt et al. 2012), while these data in SPEX are being currently updated.

Future experiments providing smaller uncertainties on measured atomic properties, accompanied by precise calculations, are needed to match the precision of X-ray microcalorimeter-type missions, in order to fully enable the range of spectral diagnostics of the Fe XVII ion.

5.4 Charge exchange

Charge exchange between ions and neutral atoms or molecules could potentially mimic the effect of resonant scattering, since it enhances the forbidden line with respect to the resonant line. However, the magnitude of the effect is expected to be small in comparison with current uncertainties. Pinto et al. (2016) applied a simple charge exchange model to the elliptical galaxy NGC 4636, concluding that it did not affect the Fe XVII spectral lines, but only lines of ions tied to colder gas, e.g. O VII. Therefore, we do not include this process in our current models.

5.5 Maximal Mach number

Deriving uncertainties on measured Mach numbers using resonant scattering probability distributions requires us to adopt a prior on the 3D Mach number range (Section 4.1). Motivated by numerical simulations and measured upper limits, we choose to consider only subsonic turbulence, $M_{\rm max} = 1$. In some cases, gas motions can be sufficiently strong to suppress the resonant scattering effect, i.e. the line ratio becomes consistent with the optically thin case. In such situations, the pdfs will be flat at large Mach numbers and our constraints will therefore depend on the assumed maximal Mach number.

This is illustrated in the right-hand side of Fig. 14, where the upper panel shows 68 per cent constraints in a peaked pdf in NGC 5813, and the lower panel shows 95 per cent lower limits in a non-peaked pdf in NGC 5044, for two different maximal Mach numbers: $M_{\rm max} = 1$ (our default) and $M_{\rm max} = 2$ (red and grey regions, respectively). The lower limit in NGC 5813 is least affected by this assumption: the difference between the default case and larger $M_{\rm max}$ is only 5 per cent (4 km s^{-1}), while the upper limit increases by 9 per cent (12 km s^{-1}). Uncertainties in other galaxies with peaked distributions behave similarly. In NGC 5044, the 2σ lower limit increases by 50 per cent (34 km s^{-1}), which is the case for most galaxies with flatter pdfs. Objects least affected are the ones with very peaked distributions, such as NGC 1404 (22 per cent/18 km s^{-1} change) and NGC 5846 (27 per cent/12 km s^{-1} change).

Note that the combined resonant scattering and line broadening pdfs (results in Figs 12 and 13) are not affected by this assumption (Section 4.2).

6 DISCUSSION

6.1 Comparison with previous measurements

Resonant scattering in three galaxies (NGC 4636, NGC 5044 and NGC 5813) has been previously examined using a similar approach, and the same data and codes, by Werner et al. (2009) and de Plaa et al. (2012). The main difference with respect to these works is in comparison of simulations and observations, and in combination of resonant scattering and line broadening constraints. Despite these differences, the results on resonant scattering are consistent with the previous works.

Our measurements also agree with estimates of total turbulent velocities in NGC 5813 from shock-width measurements (Randall et al. 2015), as well as with previous upper limits measured via line broadening with *RGS* data (Sanders, Fabian & Smith 2011; Sanders & Fabian 2013; Pinto et al. 2015).

Interestingly, the cold interstellar medium (ISM) velocity dispersions mapped with C II in the cores of NGC 4636, NGC 5044, NGC 5813 and NGC 5846, match the hot gas velocity dispersions measured in this work, supporting the argument that the cold ISM cools out of the hot gas (Werner et al. 2014).

A recent *Hitomi* measurement in the inner 30 kpc region of the Perseus cluster core (NGC 1275) showed velocity broadening of 187 ± 13 km s^{-1} and a non-thermal pressure contribution of $\sim$4 per cent (8 per cent accounting for sheer motions; Hitomi Collaboration et al. 2016). This velocity is close to the best-fitting sample values of 107^{+19}_{-15} km s^{-1} and $5.6^{+2.6}_{-1.5}$ per cent non-thermal pressure support measured in this work. The sample-averaged velocity is slightly lower than the one in Perseus, but also the regions we probe in this work are smaller (few kpc versus few 10s kpc).

Our inferred non-thermal pressure contribution is consistent with observations of the cores of other giant ellipticals (measured with a different technique in NGC 1399 and NGC 4486 by Churazov et al. 2008). Its low value encourages the use of hydrostatic equilibrium approximation for galaxy mass measurements with X-rays.

6.2 Comparison with numerical simulations

Detailed hydrodynamical simulations of AGN feedback by Gaspari, Brighenti & Temi (2012) reproduce a level of subsonic turbulence consistent with our measurements (see also Gaspari, Temi & Brighenti 2017). Within the inner few kpc, the time-averaged velocity dispersion varies from $\sim$60–200 km s^{-1} in simulations, while our typical averaged results provide velocity $\sim$93–126 km s^{-1}. Similarly, Valentini & Brighenti (2015) find hot gas velocity dispersions of 100–200 km s^{-1} in the cores of simulated massive elliptical galaxies. A somewhat different conclusion was recently reached by Yang & Reynolds (2016), where the kinetic energy in AGN feedback simulations is only $\sim$1 per cent of the gas thermal energy (we find this fraction to be $5.6^{+2.6}_{-1.5}$ per cent).

The missing element in these simulations of AGN feedback is the effect of cosmological merging, which triggers additional gas motions (as shown in galaxy cluster cosmological simulations by e.g. Lau, Kravtsov & Nagai 2009; Miniati 2014; Vazza et al. 2011).

6.3 Radiative cooling and turbulent heating balance

The inferred gas velocity values measured in all objects in our sample are comparable, and there is no detectable scatter around the best-fitting mean value (albeit with large statistical uncertainty). This may hint at a common origin of the velocity field, which could be sourced by a quasi-continuous feedback mechanism, with the most obvious candidate energy source being AGN, although additional contributions from e.g. merging activity may also be present (e.g. Ascasibar & Markevitch 2006; ZuHone, Markevitch & Johnson 2010).

If indeed turbulence is produced by a feedback activity, it is interesting to estimate whether the turbulent energy dissipation is

[6] Using the latest AtomDB ver. 3.0.7 changes results by $\sim$1 per cent.

sufficient to balance the radiative cooling. By adopting an average value of the normalized cooling function $\Lambda_n \approx 1.5 \cdot 10^{-23}$, which is representative for the temperatures and metallicities of considered galaxies, we can estimate the Mach number of turbulence M_l, associated with spatial scales of motions l, which provides the balance (Zhuravleva et al. 2014):

$$M_l = 0.13 \left(\frac{n_e}{10^{-2}\,\mathrm{cm}^{-3}}\right)^{1/3} \left(\frac{c_s}{1000\,\mathrm{km\,s}^{-1}}\right)^{-1} \left(\frac{l}{10\,\mathrm{kpc}}\right)^{1/3}. \quad (11)$$

A typical galaxy core electron number density in our sample is $0.05\,\mathrm{cm}^{-3}$ and sound speed is 450 km s^{-1}. Both the typical size of the *RGS* extraction region and the effective length along the line of sight (distance that contributes 50 per cent of the flux at a given projected radius, see Zhuravleva et al. 2012) are about ∼5 kpc. If our measured velocities are dominated by gas motions on such scale, then M_l ∼0.4 should provide the cooling–heating balance. If, instead, scale associated with the measured velocity is smaller (larger), e.g. 1 kpc (10 kpc), then M_l ∼0.2 (0.5). Our measurements give an averaged $M \sim 0.44$, meaning that the turbulence should typically be enough to offset the radiative cooling in the cores of massive elliptical galaxies.

Interestingly, we measured (or have strong hints of) weak turbulence in the most relaxed giant elliptical galaxies, NGC 4261, NGC 4472 and NGC 4649 (as identified by e.g. Werner et al. 2012), while galaxy with the largest measured velocity, NGC 1404, is very dynamically active, moving within and interacting with the ICM of the Fornax cluster (e.g. Machacek et al. 2005; Su et al. 2017). We also found a few potential exceptions in our sample, where we see the indications of an insufficient level of turbulence to balance cooling in the inner few kpc region. However, any firm conclusions require additional *RGS* data.

6.4 Further improvements

The statistical uncertainty on our measurements comes from the convolved errors from the *RGS* line flux measurements and the deprojected thermodynamic profiles from *Chandra* data. In most galaxies, the *RGS* error is the dominant one and could be reduced by acquiring additional *XMM–Newton* data. The exceptions are NGC 1316 and NGC 4636, which require deeper *Chandra* observations.

The resonant scattering signal is stronger if considered in even smaller regions, where the optical depth is the largest. However, using smaller regions leads to lower photon counts and larger statistical uncertainties. Therefore, this approach also requires additional data for most objects, except for NGC 4261, NGC 4374, NGC 4472 and NGC 5044, where current data are sufficient to maximize the scattering signal.

Ahoranta et al. (2016) studied spatial variation of the optically thin-to-thick line ratio in NGC 4636, suggesting high turbulence in the southern and low in the northern region of the galaxy. In order to perform quantitative analysis of this asymmetry, it is necessary to perform Monte Carlo simulations similar to these discussed in this paper. However, such analysis requires more complex models of the galaxy geometry, relaxing the spherical symmetry assumption, which are beyond the scope of this paper.

6.5 Future microcalorimeter-type missions

Future X-ray missions with microcalorimeter-type detectors, such as e.g. *Athena*,[7] *Lynx*,[8] and *Hitomi Recovery Mission*, should deliver large volumes of spatially resolved data with superb spectral resolution. As shown by the *Hitomi* observation of the Perseus cluster (Hitomi Collaboration et al. 2016), this will allow for direct measurements of gas bulk and turbulent velocities in the centres of clusters, directly from line widths and Doppler shifts and indirectly through resonant scattering. For cooler objects, such as galaxies, with average temperature ∼1 keV, it might still be challenging to measure velocities through line broadening with ∼2.5–5 eV resolution microcalorimeters. Typical velocity found in this work (107 km s^{-1}) causes the Fe XVII lines broadening of ∼0.5 eV, while even sonic motions would cause a sub-eV broadening in a cool, 0.75 keV gas. However, the microcalorimeter data will not suffer from the major systematic of current best instrument (*RGS*; the spatial line broadening), allowing for better resonant scattering and line broadening studies.

We show simulated *Hitomi* (left) and *Athena* (right) spectra of NGC 4636 in Fig. 15 for no turbulence (upper panels) and substantial turbulence ($M = 0.45$, as measured in this work; lower panels). Resonant scattering causes suppression in the line centre of ∼45 per cent for $M = 0$ and ∼25 per cent for $M = 0.45$, which can be clearly seen with just a 100 ks *Hitomi* or a 10 ks *Athena* observation.

7 CONCLUSIONS

In this work, we have performed a detailed analysis of the resonant scattering effect in nearby, giant elliptical galaxies, thereby constraining the turbulent velocities of the hot gas in their cores. By combining the velocity constraints from resonant scattering with upper limits from spectral line broadening, we obtain significantly improved constraints on gas velocities, Mach numbers, and non-thermal pressure support. Our analysis combines high-resolution *XMM–Newton RGS* spectra, *Chandra* imaging and numerical simulations of the resonant scattering effect in these galaxies. Our main findings are as follows:

(i) Using the resonant scattering effect only, we measure 1D turbulent velocities in the cores of four massive elliptical galaxies ranging between 0–120 km s^{-1} (3D Mach numbers 0–0.5), and place lower limits of 20–100 km s^{-1} (3D Mach numbers 0–0.5) in a further nine systems.

(ii) By combining line broadening and resonant scattering measurements, we obtain interesting velocity constraints for 13 galaxies. The sample best-fitting values are: 1D velocity dispersion ∼110 km s^{-1}, 3D Mach number ∼0.45 and non-thermal to thermal pressure fraction ∼6 per cent. The scatter around these values is rather small, consistent with zero within uncertainties.

(iii) Consistency with a single velocity supports a common gas heating mechanism in massive elliptical galaxies.

(iv) For the majority of objects the measured turbulence is enough to balance the radiative cooling, assuming conservative estimates of spatial scales associated with the measured motions.

(v) The inferred non-thermal pressure contribution in the cores of giant galaxies is encouraging for hydrostatic mass measurements.

[7] http://www.the-athena-x-ray-observatory.eu/
[8] https://wwwastro.msfc.nasa.gov/lynx/

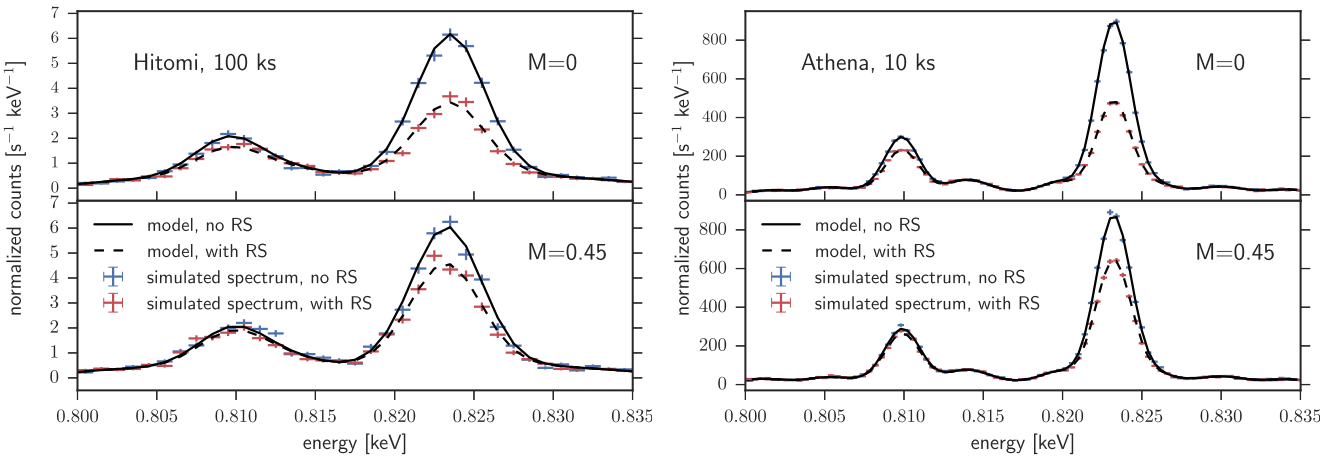

Figure 15. Simulated spectrum around the Fe XVII 15.01 Å (0.826 keV) line in the centre of NGC 4636, as would be seen by a single *Hitomi* pixel (∼5 eV resolution; left-hand panel) and by *Athena* in the same region (∼2.5 eV resolution; right-hand panel). Upper panels show the case of no turbulence, and lower panels show the case of 3D Mach number of 0.45. Dashed and solid black lines show model spectra with and without resonant scattering (RS), respectively. Red and blue points show simulated normalized photon counts for a 100 and 10 ks observation in the case of *Hitomi* and *Athena*, respectively, with and without resonant scattering. Note that for both of the instruments the spectral line broadening may be challenging to measure robustly.

(vi) In the near term, our analysis could be improved by acquiring additional *XMM–Newton* and *Chandra* data and by advancing the models.

(vii) In the long term, this approach can be used to interpret future high-resolution observations with *Hitomi Recovery Mission*, *Athena* and *Lynx*. We highlighted the major sources of systematic uncertainties, e.g. abundance measurements and atomic data, which have to be addressed to enable full exploitation of the microcalorimeter data.

ACKNOWLEDGEMENTS

This work is based on observations obtained with *XMM–Newton*, an ESA science mission funded by ESA Member States and USA (NASA). CP acknowledges support from European Research Council (ERC) Advanced Grant Feedback 340442 and new data from the awarded *XMM–Newton* proposal ID 0760870101. AO thanks J. Sanders for providing deprojected data for NGC 4696.

REFERENCES

Ahoranta J., Finoguenov A., Pinto C., Sanders J., Kaastra J., de Plaa J., Fabian A., 2016, A&A, 592, A145
Anders E., Grevesse N., 1989, Geochim. Cosmochim. Acta, 53, 197
Ascasibar Y., Markevitch M., 2006, ApJ, 650, 102
Bernitt S. et al., 2012, Nature, 492, 225
Bregman J. N., Miller E. D., Athey A. E., Irwin J. A., 2005, ApJ, 635, 1031
Brown G. V., Beiersdorfer P., Chen H., Chen M. H., Reed K. J., 2001, ApJ, 557, L75
Brown G. V. et al., 2006, Phys. Rev. Lett., 96, 253201
Brüggen M., Ruszkowski M., Hallman E., 2005, ApJ, 630, 740
Bryans P., Landi E., Savin D. W., 2009, ApJ, 691, 1540
Buote D. A., Lewis A. D., Brighenti F., Mathews W. G., 2003, ApJ, 595, 151
Churazov E., Forman W., Jones C., Böhringer H., 2003, ApJ, 590, 225
Churazov E., Forman W., Jones C., Sunyaev R., Böhringer H., 2004, MNRAS, 347, 29
Churazov E., Forman W., Vikhlinin A., Tremaine S., Gerhard O., Jones C., 2008, MNRAS, 388, 1062
Churazov E., Zhuravleva I., Sazonov S., Sunyaev R., 2010, Space Sci. Rev., 157, 193
de Plaa J. et al., 2017, A&A, preprint (arXiv:1707.05076)
de Plaa J., Mernier F., 2016, Astron. Nachr., 338, 299
de Plaa J., Zhuravleva I., Werner N., Kaastra J. S., Churazov E., Smith R. K., Raassen A. J. J., Grange Y. G., 2012, A&A, 539, A34
Dullo B. T., Graham A. W., 2014, MNRAS, 444, 2700
Faber S. M., Wegner G., Burstein D., Davies R. L., Dressler A., Lynden-Bell D., Terlevich R. J., 1989, ApJS, 69, 763
Fabian A. C., Sanders J. S., Taylor G. B., Allen S. W., Crawford C. S., Johnstone R. M., Iwasawa K., 2006, MNRAS, 366, 417
Fabian A. C., Walker S. A., Russell H. R., Pinto C., Sanders J. S., Reynolds C. S., 2017, MNRAS, 464, L1
Foster A. R., Ji L., Smith R. K., Brickhouse N. S., 2012, ApJ, 756, 128
Gaspari M., Brighenti F., Temi P., 2012, MNRAS, 424, 190
Gaspari M., Temi P., Brighenti F., 2017, MNRAS, 466, 677
Gastaldello F., Molendi S., 2004, ApJ, 600, 670
Gilfanov M. R., Syunyaev R. A., Churazov E. M., 1987, Sov. Astron. Lett., 13, 3
Guo F., Oh S. P., 2008, MNRAS, 384, 251
Hamilton D. R., 1947, ApJ, 106, 457
Hillel S., Soker N., 2016, MNRAS, 455, 2139
Hitomi Collaboration et al., 2016, Nature, 535, 117
Hu J., 2008, MNRAS, 386, 2242
Jacob S., Pfrommer C., 2017, MNRAS, 467, 1478
Kaastra J. S., Mewe R., Nieuwenhuijzen H., 1996, in Yamashita K., Watanabe T., eds, UV and X-ray Spectroscopy of Astrophysical and Laboratory Plasmas. Universal Academy Press, Tokyo, p. 411
Kim W.-T., Narayan R., 2003, ApJ, 596, 889
Kormendy J., Fisher D. B., Cornell M. E., Bender R., 2009, ApJS, 182, 216
Kunz M. W., Schekochihin A. A., Stone J. M., 2014, Phys. Rev. Lett., 112, 205003
Laganá T. F., Lovisari L., Martins L., Lanfranchi G. A., Capelato H. V., Schellenberger G., 2015, A&A, 573, A66
Lau E. T., Kravtsov A. V., Nagai D., 2009, ApJ, 705, 1129
Loubser S. I., Sansom A. E., Sánchez-Blázquez P., Soechting I. K., Bromage G. E., 2008, MNRAS, 391, 1009
Machacek M., Dosaj A., Forman W., Jones C., Markevitch M., Vikhlinin A., Warmflash A., Kraft R., 2005, ApJ, 621, 663
Ma C.-P., Greene J. E., McConnell N., Janish R., Blakeslee J. P., Thomas J., Murphy J. D., 2014, ApJ, 795, 158
Mernier F. et al., 2017, A&A, 603, 80

Miniati F., 2014, ApJ, 782, 21
Misgeld I., Hilker M., Mieske S., 2009, A&A, 496, 683
Nulsen P. E. J., Fabian A. C., 2000, MNRAS, 311, 346
Panagoulia E. K., Sanders J. S., Fabian A. C., 2015, MNRAS, 447, 417
Pinto C. et al., 2015, A&A, 575, A38
Pinto C. et al., 2016, MNRAS, 461, 2077
Randall S. W. et al., 2015, ApJ, 805, 112
Roediger E., Kraft R. P., Nulsen P., Churazov E., Forman W., Brüggen M., Kokotanekova R., 2013, MNRAS, 436, 1721
Rusli S. P., Thomas J., Erwin P., Saglia R. P., Nowak N., Bender R., 2011, MNRAS, 410, 1223
Ruszkowski M., Yang H.-Y. K., Reynolds C. S., 2017, ApJ, 844, 12
Saglia R. P., Burstein D., Baggley G., Davies R. L., Bertschinger E., Colless M. M., McMahan R. K., Jr, Wegner G., 1997, MNRAS, 292, 499
Sanders J. S., Fabian A. C., 2013, MNRAS, 429, 2727
Sanders J. S., Fabian A. C., Smith R. K., 2011, MNRAS, 410, 1797
Sanders J. S. et al., 2016, MNRAS, 457, 82
Sazonov S. Y., Churazov E. M., Sunyaev R. A., 2002, MNRAS, 333, 191
Scannapieco E., Brüggen M., 2008, ApJ, 686, 927
Shigeyama T., 1998, ApJ, 497, 587
Sijacki D., Springel V., Di Matteo T., Hernquist L., 2007, MNRAS, 380, 877
Sijacki D., Pfrommer C., Springel V., Enßlin T. A., 2008, MNRAS, 387, 1403
Smith R. K., Brickhouse N. S., Liedahl D. A., Raymond J. C., 2001, ApJ, 556, L91
Spavone M., Iodice E., Longo G., Paolillo M., Sodani S., 2006, A&A, 457, 493
Su Y. et al., 2017, ApJ, 834, 74
Temi P., Mathews W. G., Brighenti F., 2005, ApJ, 622, 235
Valentini M., Brighenti F., 2015, MNRAS, 448, 1979
Vazza F., Brunetti G., Gheller C., Brunino R., Brüggen M., 2011, A&A, 529, A17
Vikhlinin A., Markevitch M., Murray S. S., Jones C., Forman W., Van Speybroeck L., 2005, ApJ, 628, 655
Walker S. A., Sanders J. S., Fabian A. C., 2015, MNRAS, 453, 3699
Weinberger R. et al., 2017, MNRAS, 465, 3291
Werner N., Zhuravleva I., Churazov E., Simionescu A., Allen S. W., Forman W., Jones C., Kaastra J. S., 2009, MNRAS, 398, 23
Werner N., Allen S. W., Simionescu A., 2012, MNRAS, 425, 2731
Werner N. et al., 2014, MNRAS, 439, 2291
Xu H. et al., 2002, ApJ, 579, 600
Yang H.-Y. K., Reynolds C. S., 2016, ApJ, 829, 90
Zhuravleva I. V., Churazov E. M., Sazonov S. Y., Sunyaev R. A., Forman W., Dolag K., 2010, MNRAS, 403, 129
Zhuravleva I. V., Churazov E. M., Sazonov S. Y., Sunyaev R. A., Dolag K., 2011, Astronomy Letters, 37, 141
Zhuravleva I., Churazov E., Kravtsov A., Sunyaev R., 2012, MNRAS, 422, 2712
Zhuravleva I. et al., 2014, Nature, 515, 85
ZuHone J. A., Markevitch M., Johnson R. E., 2010, ApJ, 717, 908

APPENDIX A: RESONANT SCATTERING RESULTS FOR THE REMAINDER OF THE SAMPLE

In Fig. A1, we present resonant scattering-only results for the remaining galaxies, which have not been shown in the main text. For details, see Section 4.1.

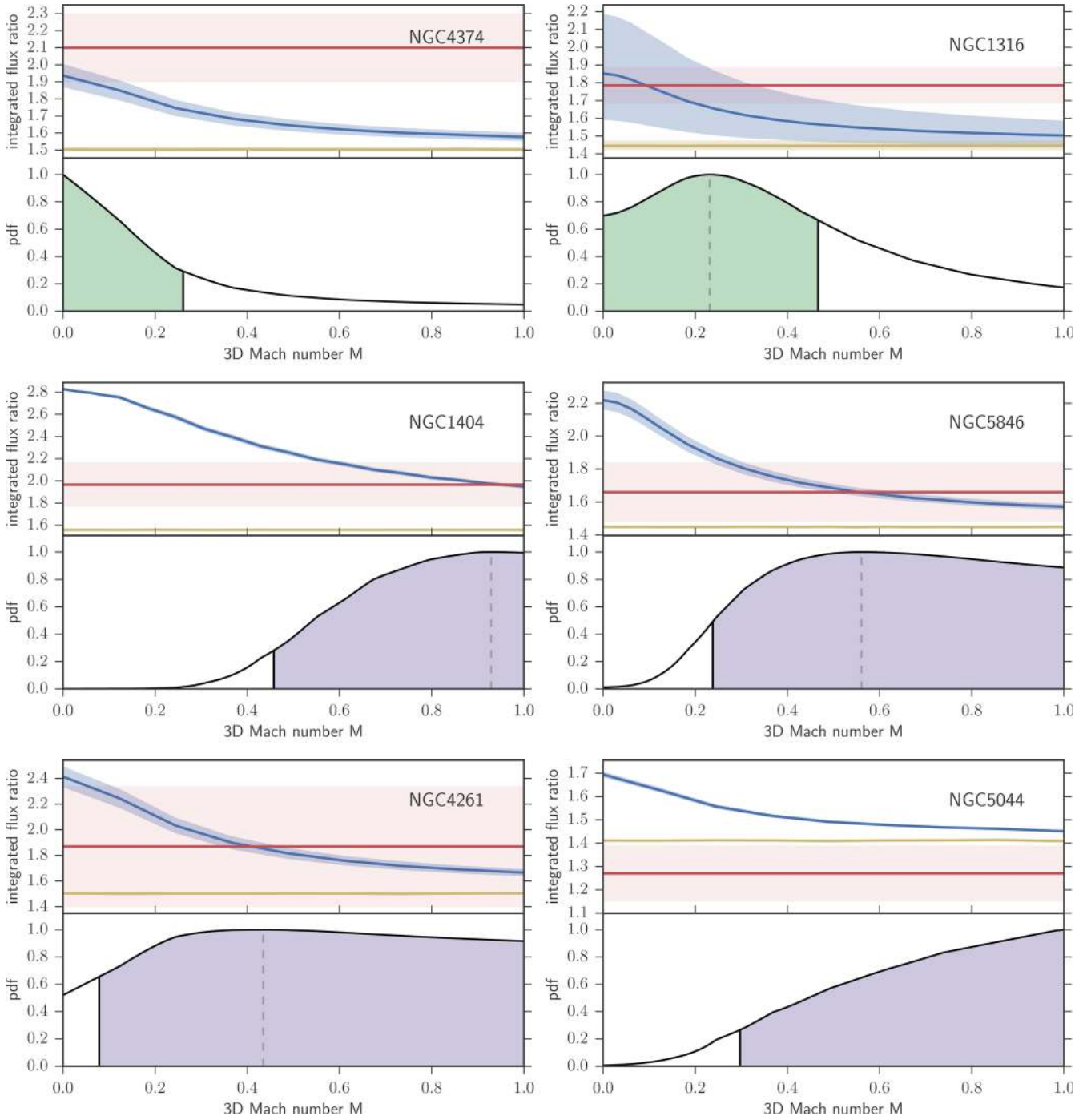

Figure A1. Results for the remaining galaxies in our sample. Upper panels: comparison of the observed flux ratio (red line) with one simulated given different turbulent motions (blue line; see Section 3.4 for details). The limit of optically thin lines is shown in yellow. Respective colored regions show 1σ uncertainties. Lower panels: Mach number probability density function resulting from convolution of models and data shown in upper panel. Grey dashed line shows the most probable value, while green and purple regions mark the 1σ and 2σ constraints, respectively. The figure continues on to the next page. See Section 4.1 for details.

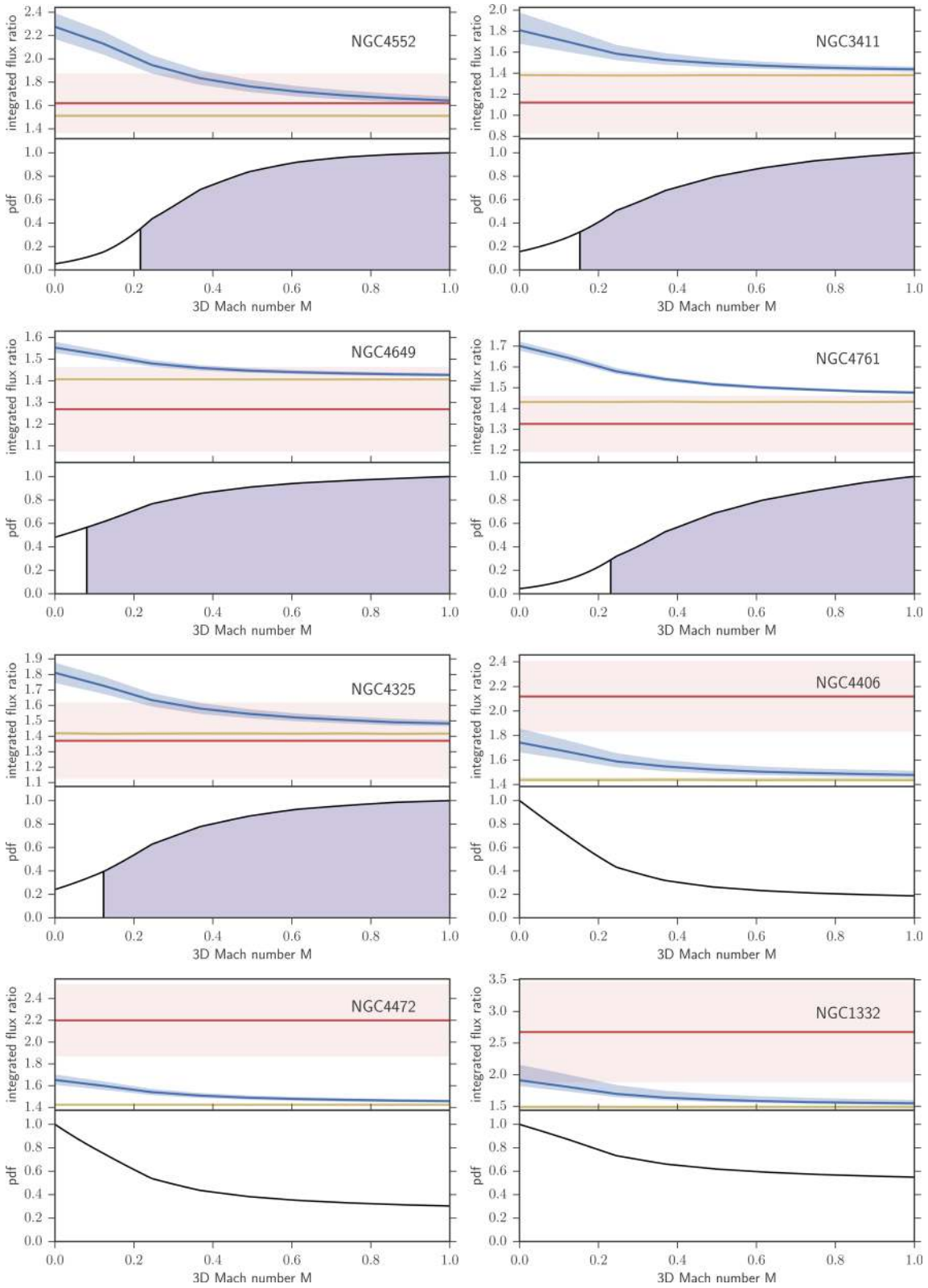

Figure A1 – *continued*

This paper has been typeset from a TEX/LATEX file prepared by the author.